nature neuroscience

Article

https://doi.org/10.1038/s41593-025-02155-2

Genetic mapping identifies *Homer1* as a developmental modifier of attention

Received: 24 June 2024

Accepted: 23 October 2025

Zachary Gershon[1], Alessandra Bonito-Oliva[1], Matt Kanke[2], Andrea Terceros[1], Genelle Rankin[1], John Fak[1], Yujin Harada[1], Andrew F. Iannone[3], Millennium Gebremedhin[1], Brian Fabella[4], Natalia V. De Marco García[3], Praveen Sethupathy[2] & Priya Rajasethupathy[1] ✉

The genetic factors and resulting neural circuit physiology driving variation in attention are poorly understood. Here we took an unbiased forward genetics approach to identify genes of large effect on attention. We studied 200 genetically diverse mice and, through genetic mapping, identified a small locus on chromosome 13 (95% CI 92.22–94.09 Mb) that is significantly associated with variation in pre-attentive processing. Within the locus we identified a gene, *Homer1*, encoding a synaptic protein, whose downregulation during development led to improvements in multiple measures of attention in adulthood. Mechanistically, reduced *Homer1* levels resulted in an upscaling of GABA receptors and enhanced inhibitory tone in the prefrontal cortex, leading to improved neural signal to noise and attentional performance. We thus identify a single genetic locus of large effect on attention and propose *Homer1*-dependent inhibitory tone, sculpted during a developmental sensitive period, as a key regulator and potential therapeutic target for attentional performance.

Animals are bombarded with a constant stream of sensory inputs but have limited capacity with which to process them. A mechanism for filtering, prioritizing and directing mental assets is required to prevent sensory overload and enable meaningful comprehension; this process of sensory selection and prioritization is described as attention[1–3]. Years of foundational research have highlighted the importance of the prefrontal cortex in mediating attentional control. The prefrontal cortex (PFC) receives sensory inputs, as well as measures of internal state, value and goals, by which it is thought to be well positioned to prioritize relevant inputs to direct attentional resources. Indeed, many attention-deficit hyperactivity disorder (ADHD) medications work in the PFC to boost attentional performance[4]; however, the genetic factors and resulting neural circuit physiology that drives variation in this trait are not well understood.

In the past, genetic mapping approaches enabled the unbiased identification of genes with prominent contributions to a behavioral trait[5–11]. Further investigations of these genes provided entry points to develop cellular models that link physiology and behavior. Toward this goal, we previously performed genetic mapping in outbred mice and identified a single gene of large effect on short-term memory[12]. Building on this platform, here we performed a large-scale study in outbred mice to understand the sources of variation in pre-attentive processing and attentional performance. Through genetic mapping, we identified a genetic locus on chromosome 13 linked to variation in these traits. Further characterization of genes within the locus revealed that *Homer1*, whose transcripts encode a synaptic protein, causally affects attention. In particular, downregulation of *Homer1* in the PFC during an early developmental sensitive period led to improvements in multiple measures of attention in the adult. Subsequent mechanistic studies revealed that prefrontal *Homer1* downregulation leads to GABAergic receptor upregulation and strong inhibitory tone. This was observed as substantially diminished PFC activity at baseline periods of the task, but targeted elevations at cue onset, leading to short-latency correct behavioral choices. We thus characterize a gene of large effect

---

[1]Laboratory of Neural Dynamics & Cognition, The Rockefeller University, New York, NY, USA. [2]Department of Biomedical Sciences, Cornell University, Ithaca, NY, USA. [3]Feil Family Brain and Mind Research Institute, Weill Cornell, New York, NY, USA. [4]Laboratory of Sensory Neuroscience, The Rockefeller University, New York, NY, USA. ✉e-mail: priya@rockefeller.edu

https://doi.org/10.1038/s41593-025-02155-2

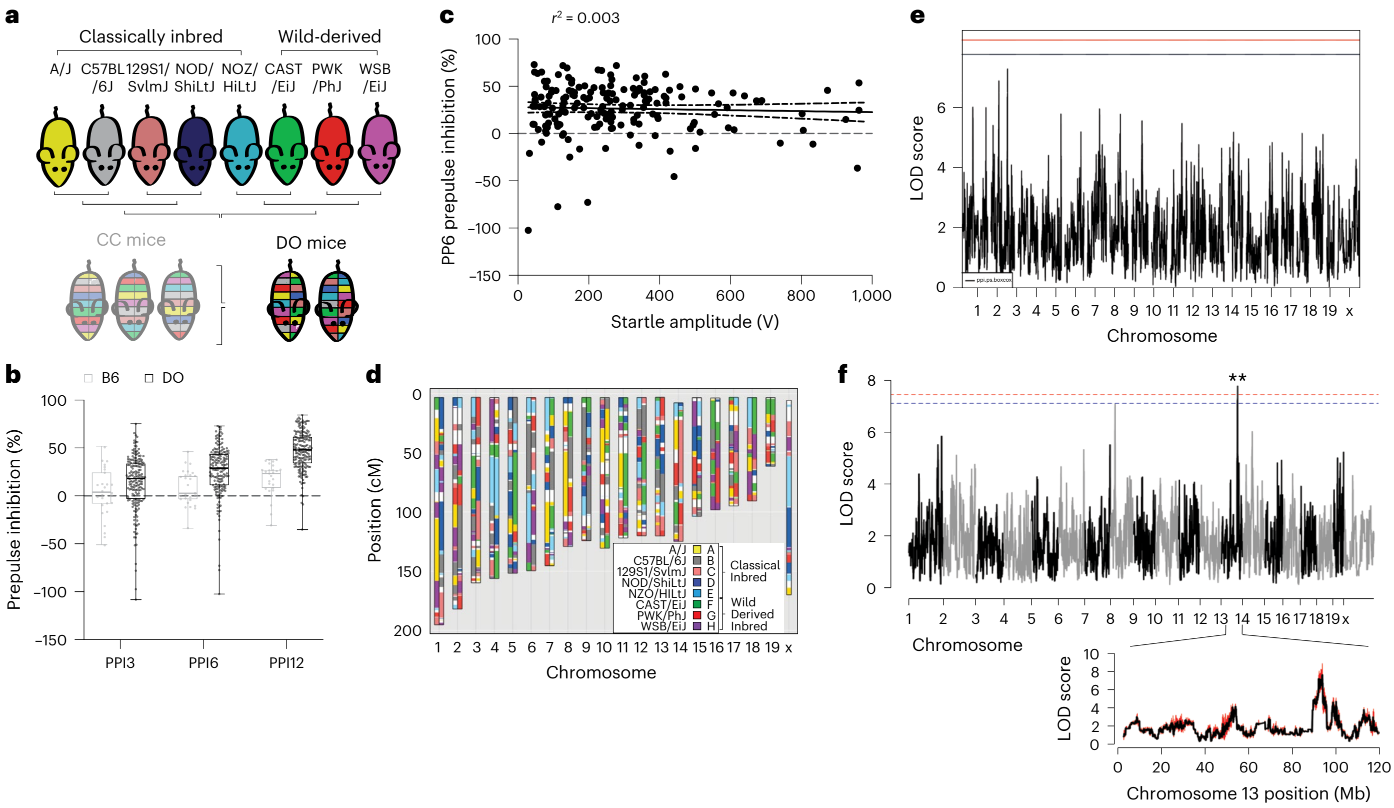

Fig. 1 | Identification of a QTL associated with pre-attentive processing. **a**, Outbreeding scheme to generate the DO mice. **b**, Pre-attentive processing performance (assayed by PPI) in B6 ($n = 27$) and DO ($n = 176$) mice measured as percent of startle response inhibited at three different prepulse intensities: 3, 6 and 12 dB above background (PPI3, 6 and 12, respectively). Upper and lower box limits indicate 75th and 25th percentiles, center line indicates the median and upper and lower whiskers are the maximum and minimum data points. **c**, Correlation in DO mice ($n = 176$) between startle response, measured as the magnitude of startle amplitude (V) and PPI, measured as percent inhibition, at 6 dB above background (PP6, $r^2 = 0.003$). **d**, Haplotype reconstruction of a representative DO mouse from the 25th generation of the population. Colors correspond to the founder lines (shown in legend) for which the genomic contribution is attributed at each depicted locus. **e**, QTL mapping analysis of startle response (by R/qtl2) shown as a Manhattan plot of startle response. Blue and red lines indicate confidence thresholds (blue, 90% and red, 95%). **f**, QTL analysis (by miQTL) for PPI at 6 dB above background (PPI6) (top). Confidence thresholds after 50 imputations of genotype (blue, 90% and red, 95%). Genome-wide two-sided $P < 0.01$, 19% variance explained. Mapping analyses performed using R/qtl2 (black) and miQTL (red) revealing minimal fluctuation in LOD score across imputations (overlapping bands) (bottom).

on attention (*Homer1*) and highlight prefrontal inhibitory tone as an important source of variation that predicts neural signal-to-noise and attentional performance.

Identification of a QTL linked to pre-attentive processing

The diversity outbred (DO) resource is a mouse population derived from eight founder strains, whose genetic diversity, including single-nucleotide polymorphism (SNP) density and allelic heterozygosity, is comparable to that of the human population, providing a platform for high-resolution genetic mapping (Fig. 1a). Indeed, we and others have used this resource[12–15] and other outbred or genetically diverse cohorts[16,17] to powerfully map genetic variation to trait variation. Notably, genetic mapping can be most successful if the screening behaviors are simple, innate and robustly quantifiable[15,18]. As traditional tasks of attention require extensive training (often 3–6 weeks), reward associations and other potential confounds for genetic mapping, we selected and optimized an assay for innate pre-attentive processing (prepulse inhibition (PPI) of startle response). This behavioral process of PPI refers to the natural response of mice to startle when presented with a sudden strong (often auditory) stimulus, and furthermore, the ability of the animal to suppress the startle when the strong stimulus is directly preceded by a weaker stimulus. This is thought to reflect the process of neural filtering of redundant or irrelevant stimuli while enhancing the subsequent goal-directed processing of salient aspects of the environment[19]. Extensive previous work has characterized PPI as a pre-attentive process[20–24], identifying significant overlaps in the neural circuits mediating PPI and attentional control[25–27], and additional studies have linked it to measures of attention in rodents and humans[28–31]. While PPI can also reflect changes in sensory, motor and anxiety measures (which we tested post hoc), it served as a sensitive initial screen, which we then followed with more-targeted assays for attention.

Based on our previous work[12] and power estimates (Methods), we aimed to test 200 mice for performance in PPI. In brief, for each DO mouse we measured the startle response to a 120 dB tone as well as the percent inhibition of this startle when preceded by a weaker 3, 6 or 12 dB tone (PPI3, PPI6 and PPI12). We first confirmed that the phenotypic variability of the DO greatly surpassed that of the C57BL/6J (B6) classical inbred line (*F*-test of mean PPI measures, $P = 0.02$), as would be expected from the underlying genetic variation (Fig. 1b). We lost 9 mice to poor health before testing and excluded 15 mice during testing that exhibited potential hearing impairment (Methods). Overall, we found no significant correlations between PPI and startle response or body weight (Fig. 1c and Extended Data Fig. 1a–d).

We next genotyped the 176 DO mice using the GigaMUGA platform (114,184 loci had variability in our cohort). Founder haplotype reconstructions were performed with a hidden Markov model[12,32], which showed extensive allelic heterozygosity (Fig. 1d) and we observed approximately equal founder contributions across our cohort suggesting minimal allelic loss. We performed quantitative trait loci (QTL) mapping using R/qtl2 (ref. 32) and identified a single genetic locus on chromosome 13 linked to variation in PPI, with genome-wide significance of $P \leq 0.01$ (Extended Data Fig. 1e; logarithm of odds (LOD) score for PPI6 = 8.22, 95% CI 92.22–94.09 Mb). These mapping effects were not due to individual differences in the underlying innate startle response (Fig. 1c), nor was there any QTL detected when mapping to startle scores (Fig. 1e). The chromosome 13 QTL for PPI6 was also confirmed to be statistically significant using a second mapping approach, miQTL (Fig. 1f). QTL mapping of PPI3 and PPI12 did not reveal any loci that surpassed significance thresholds (potentially due to floor and ceiling effects in the behavior), but a suggested peak for PPI3 indeed mapped to the same Chr13 QTL (Extended Data Fig. 1e), supporting the functional significance of this locus. Of note, as we performed the QTL analysis solely with males, subsequent experiments were performed using mixed-sex cohorts (Figs. 2 and 4) to confirm that sex differences do not contribute to these behavioral differences.

Next, to further increase confidence that variation at this locus is linked to variation in PPI we performed an allele effect analysis (Methods) and found that the B6 haplotype (henceforth referred to as Chr13 QTL^{B6}) was associated with high performance (high PPI scores), whereas the WSB/EiJ haplotype (henceforth referred to as Chr13 QTL^{WSB}) was associated with low performance (Fig. 2a,b). We then asked whether recombinant inbred collaborative cross (CC) lines, which have the same multiparent origins as the DO (Fig. 2c), which possess either Chr13 QTL^{B6} or Chr13 QTL^{WSB} would separate into high and low performers, respectively. After analyzing the genomes of existing CC lines, we selected three that were homozygous for each of our desired Chr13 QTL^{B6} (CC002, CC051, and CC083) or Chr13 QTL^{WSB} (CC025, CC035, and CC038) haplotypes while maintaining distinctive mosaic representations of the founder genomes at other loci. We compared PPI performance between three CC lines with the Chr13 QTL^{B6} diplotype and the three with the Chr13 QTL^{WSB} diplotype and found that all three Chr13 QTL^{B6} lines have significantly greater PPI than each of the Chr13 QTL^{WSB} lines (Fig. 2d,e; two-way analysis of variance (ANOVA) $P < 0.001$). As with the DO, this finding was not explained by differences in peak startle or body weight (Extended Data Fig. 2a–d). These data increase confidence that genetic variation at the Chr13 locus, specifically the WSB versus B6 haplotype, explains significant variation in PPI.

As PPI screens for pre-attentive processing, which is well associated with but does not directly test attention, we next assessed the role of the Chr13 QTL in attention. To do so, we selected one high-performing (B6 haplotype) and one low-performing (WSB haplotype) line (CC025 and CC083), for follow-up attentional testing using an operant signal detection task (SDT) (Fig. 2f). Here, mice are trained to nosepoke in response to a 5-s auditory cue within 10 s of cue onset to receive a food reward. Once the mice have sufficiently learned the task (Methods), their attentional load is then challenged by decreasing the length of the cue to 1 s and reducing the response window (Fig. 2g,h). Similar SDTs have been widely used to assay attention[33–35]. They provide multiple metrics to track attention, with the most important measure being response latencies on correct trials once mice have learned the task, which avoid confounds related to overall differences in motivation or learning. Since acoustic startle response, PPI and SDT require intact hearing and motor ability, we first tested these mice to ensure there were no differences in hearing sensitivity, gross motor activity or motor coordination (Extended Data Fig. 2e–g). We additionally confirmed that there were also no innate differences in task-associated motor functions or motivational differences (Extended Data Fig. 2h,i).

During the initial 5-s cue training, there were no significant differences in learning the task, but CC083 mice were already exhibiting fast latency responses, and after increased attentional load during the 1-s trials, the CC083s significantly outperformed the CC025s in all of the measures of attention including accuracy, proportion of omissions, and, most significantly, latency to correct responses (Fig. 2i–k). Notably, once the CC mice performed above chance (session 6, Fig. 2i), the CC083 mice continued to respond faster than the CC025 (Fig. 2k), demonstrating better attention in a learning-independent manner. The lines did not differ in other cognitive, motivational or social measures that we tested (Extended Data Fig. 2j–l). We did observe differences in measures of anxiety-related behavior (Extended Data Fig. 2m,n), which requires further consideration given the important dependencies between anxiety and attention (although of note, in later experiments, when manipulating only a gene within this locus that causally mediates pre-attentional and attentional processing, no significant differences in anxiety-like behavior was observed). Together, these data suggest that genetic variation at the chromosome 13 locus drives differences in attentional performance.

Chr13 QTL effects on attention are phenocopied by manipulation of *Homer1*

We next sought to understand which gene(s) was driving the changes in attentional performance. The causal variants at this locus could be coding mutations that affect protein structure and/or function. They could also be noncoding mutations that affect the expression of genes within the locus, or even distal genes beyond the locus. As a starting point for the analysis, we performed bulk RNA sequencing (RNA-seq) in DO high and low performers (Fig. 3a), focusing on the PFC because of its central role in attentional processing, but also including related brain areas such as the mediodorsal thalamus (MD) and the ventral tegmental area (VTA) because of their overlapping importance in pre-attentive and attentional processing. We found that samples stratified by performance in PFC and MD, but not in VTA (Extended Data Fig. 3a), leading us to first ask whether genes within the chromosome 13 locus (Extended Data Fig. 3b) were differentially expressed (DE) in MD or PFC between high and low performers. Of all locus genes, only *Homer1* was significantly DE, with substantial downregulation in PFC in high performers (Fig. 3b; adjusted $P < 0.001$). *Homer1* has several transcript variants due to alternative splicing (Extended Data Fig. 3c)[36], and thus we assessed whether differential expression was uniform across splice isoforms. Notably, only the short, activity-dependent isoforms, *Homer1a*[37,38] and *Ania3* (ref. 36), were DE between DO high and low performers (Fig. 3c; P(*Homer1a*) = 0.003, P(*Ania3*) = 0.007, two-way ANOVA with post hoc Holm–Sidak test for multiple comparisons). Furthermore, bulk RNA sequencing also confirmed significant *Homer1* downregulation in the high-performing (CC083) compared to the low-performing (CC025) CC line (Fig. 3d,e). As with the DO mice, the differential *Homer1* expression in CC mice was driven by downregulation of *Homer1a* and *Ania3* short isoforms in the high-performing CC083s (Fig. 3f; two-way ANOVA $P < 0.001$, Holm–Sidak test for multiple comparisons P(*Homer1a*) < 0.001, P(*Ania3*) < 0.001). Based on these initial noteworthy data, although in theory the expression of distal genes could also be affected by noncoding variants in the locus of interest, we decided to focus on *Homer1a*/*Ania3* for further study.

We asked whether *Homer1a* manipulations[36,39] could drive behavioral changes in attentional performance. To knock down *Homer1a*, we designed and tested AAV-based short-hairpin RNAs (shRNAs) to target the *Homer1a* isoform in vitro and selected the most effective shRNA (Extended Data Fig. 3d,e) for bilateral PFC injections in vivo and behavioral testing (Fig. 3g–j and Extended Data Fig. 3f). To overexpress *Homer1a*, which has endogenous expression primarily in excitatory pyramidal neurons, we cloned the *Homer1a* coding sequence into an AAV-based CaMKII–eYFP vector (Extended Data Fig. 3g) for bilateral PFC injection and behavioral testing (Fig. 3k–n and Extended Data Fig. 3i,j). Of note, we did not observe any significant behavioral effect for either the knockdown or overexpression experiments (Fig. 3j,n and Extended Data Fig. 3f–h). To account for potential functional redundancy of Homer1a through Ania3, we performed bilateral PFC injections of the AAV shRNA targeting *Homer1a* pooled together with an AAV-based shRNA for *Ania3* (Extended Data Fig. 3k,l), which we

https://doi.org/10.1038/s41593-025-02155-2

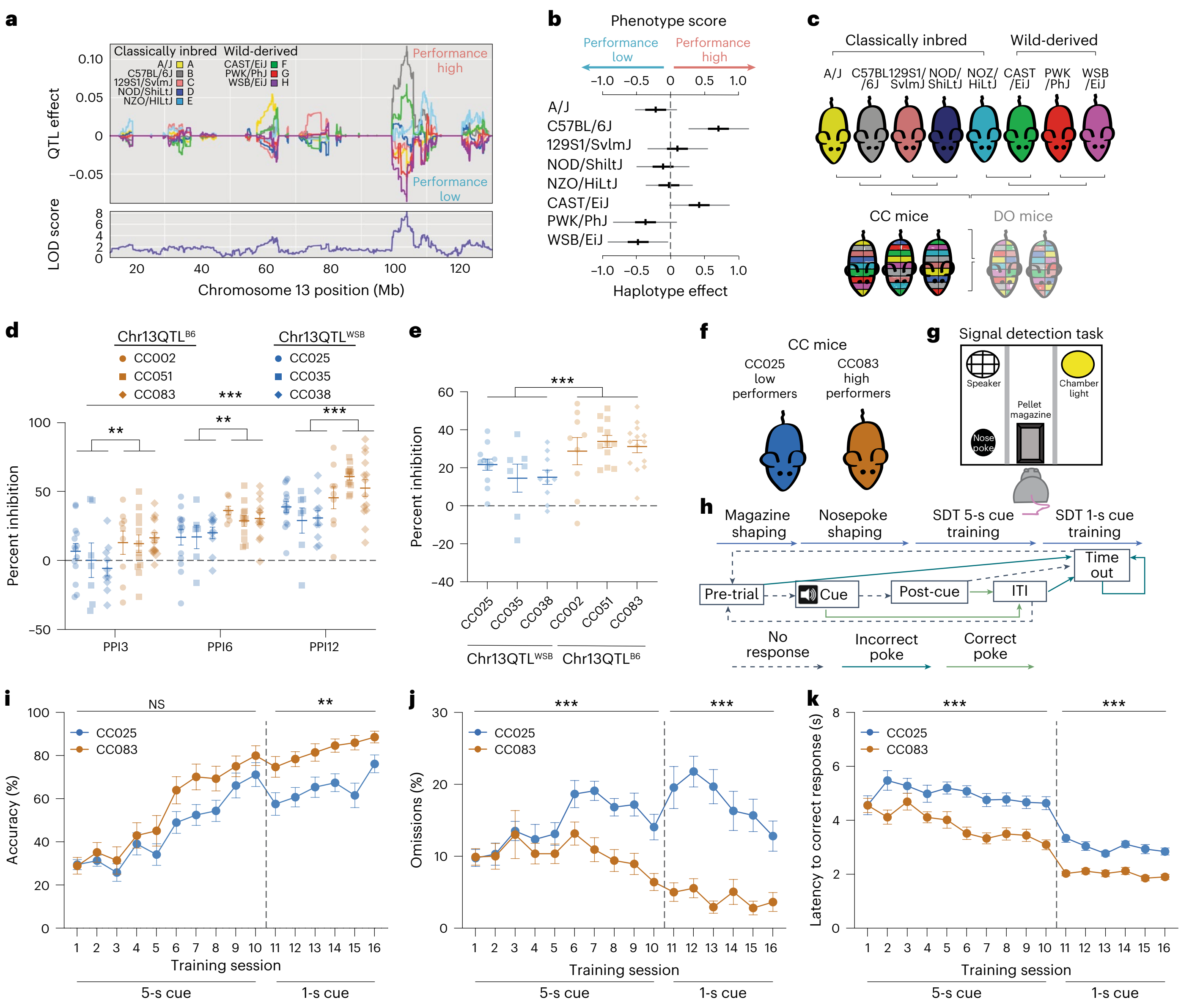

Fig. 2 | Chr13 QTL mediates variation in attentional performance. **a**, Effect of each founder allele on PPI performance along chromosome 13, as measured by founder coefficients from the linkage model. Coefficients diverge substantially at peak QTL. The LOD score at each chromosomal position is shown. **b**, Haplotype representation at the chromosome 13 locus and corresponding *z*-scored phenotypes of each founder strain, quantified as mean ± 95% CIs. **c**, Outbreeding scheme to generate the CC mice. **d**, PPI3, 6 and 12 values for three CC lines with the Chr13 QTL^{WSB} (low-performing) diplotype, CC025 ($n = 7$ M + 7 F), CC035 ($n = 3$ M + 6 F) and CC038 ($n = 6$ M + 6 F) and three CC lines with the Chr13 QTL^{B6} (high-performing) diplotype, CC002 ($n = 6$ M + 6 F), CC051 ($n = 6$ M + 6 F) and CC083 ($n = 7$ M + 7 F). Two-way ANOVA $P < 0.0001$ for haplotype main effect followed by Holm–Sidak's test for multiple comparisons $P_{\text{PPI3}} = 0.0076$, $P_{\text{PPI6}} = 0.0056$ and $P_{\text{PPI12}} = 0.0001$, no significant interaction between sex and haplotype by three-way ANOVA. **e**, Global PPI, averaging PPI3, 6 and 12 values for each mouse, in three CC lines with the Chr13 QTL^{WSB} diplotype, CC025 ($n = 6$ M + 6 F), CC035 ($n = 6$ M + 3 F) and CC038 ($n = 6$ M + 6 F) and three CC lines with the Chr13 QTL^{B6} diplotype, CC002 ($n = 6$ M + 6 F), CC051 ($n = 6$ M + 6 F) and CC083 ($n = 7$ M + 7 F). Two-way unpaired *t*-test between haplotypes $P = 0.0003$, no interaction between sex and haplotype by two-way ANOVA. **f**, Cartoon of the CC025 (low performers, blue) and CC083 (high performers, tan) used in subsequent experiments. **g**, Schematic of the operant wall of the arena used for the SDT. **h**, Schematic of SDT protocol. **i**–**k**, Performance of CC025 ($n = 11$ male (M) + 12 female (F) for 5-s cue and $n = 9$ M + 9 F for 1-s cue) and CC083 ($n = 11$ M + 12 F for 5 s cue and $n = 10$ M + 11 F 1 s cue) mice during SDT across sessions, showing accuracy (correct response) percentage (repeated-measures two-way ANOVA $P = 0.0011$ for CC line main effect in 1 s cue sessions) (**i**), percentage of omitted trials (repeated-measures two-way ANOVA p0.0007 for CC line main effect in 5 s cue sessions and $P < 0.0001$ for CC line main effect in 1-s cue sessions) (**j**) and mean latency from cue to first response within correct trials (repeated-measures two-way ANOVA $P < 0.0001$ for CC line main effect in both 5-s and 1-s cue sessions) (**k**). NS, not significant. No significant interaction between sex and CC line by repeated-measures three-way ANOVAs for accuracy (**i**), omissions (**j**) and correct response latency (**k**). Data in **d**,**e**,**i**–**k** are expressed as mean ± s.e.m.

validated in vitro (Extended Data Fig. 3i,j), and again saw no significant behavioral effect (Extended Data Fig. 3m,n).

To assess whether the effects of *Homer1a* may be developmental, we profiled the expression of *Homer1a*, *Ania3* and *Homer1b/c* in CC083 and CC025 mice across postnatal development (Fig. 4a). We found that the expression of *Homer1a* and *Ania3*, but not that of *Homer1b/c*, diverged between the CC lines as early as p14–p21 (Fig. 4b; two-way ANOVA $P = 0.02$), suggesting possible developmental roles in regulating attentional control. To test this hypothesis, we knocked down *Homer1a* and *Ania3* during early developmental stages (p14–p21) by bilaterally injecting the pooled *Homer1a* and *Ania3* shRNA AAVs into the PFC of neonatal B6 pups (Fig. 4c; referred to as KD_{dev}). Despite the developmental *Homer1a* knockdown being less effective than the adult manipulation (~80% in adults and ~60% in pups; Fig. 3i and Extended Data Fig. 4a–c), we observed significant improvement in measures of pre-attentive processing (PPI; Fig. 4d).

We tested the effects of developmental *Homer1a/Ania3* perturbations in more specific tests of attention. We applied several widely used assays for attention, including (1) an operant SDT (Fig. 4e–h); (2) a Go/No-Go task (Fig. 4i–m); (3) a head-fixed multimodal SDT (Extended Data Fig. 4m–o); and (4) an attentional set shift task[39] (Extended Data Fig. 4p,q). We ran these experiments double-blinded wherever possible, and notably, in all cases, we observed a substantial improvement in attentional performance in mice with developmental prefrontal *Homer1/Ania3* knockdown compared to controls. For instance, on the operant SDT task, while there were no differences in their innate task-related motor function, motivation or overall ability to learn the task (Fig. 4 and Extended Data Fig. 4h,i), KD_{dev} mice exhibited significantly faster response latencies than controls, particularly on correct trials, which persisted throughout the extent of both cue length phases (Fig. 4g,h; repeated-measures two-way ANOVA P(5-s cue) = 0.035, P(1-s cue) < 0.0001). Furthermore, in a head-fixed Go/No-Go task where mice were trained to respond to one paired tone or odor cue and inhibit response to a different paired tone or odor cue (Fig. 4i), again, there were no overall differences in learning (Fig. 4j) but KD_{dev} mice responded faster (Fig. 4k,l) and more reliably (Fig. 4m) than Scramble controls. Notably, the magnitudes of these effect sizes were substantial, for instance, with mean differences in response latency between groups of ~500 ms on the operant SDT task (~2.5 s for Scramble controls versus 2.0 s for KD_{dev}, $P < 0.0001$ by two-way ANOVA; Fig. 4h) and ~150 ms for the head-fixed Go/No-Go task (~650 ms for Scramble controls versus 500 ms for KD_{dev}, $P < 0.005$ by two-way ANOVA; Fig. 4l and appreciable qualitatively in the raw lick rasters in Fig. 4k).

We also performed control experiments to assess the sensory or motor confounds to the observed differences in pre-attentive (Extended Data Fig. 4h–l) and attentional processing (Extended Data Fig. 4m–q). As with CC mice, KD_{dev} and controls displayed no significant differences in gross motor control, motor coordination or hearing (Extended Data Fig. 4h–j), nor did they display broad cognitive deficits (Extended Data Fig. 4r,s). Notably, however, in contrast to CC mice, they exhibited no significant differences in anxiety-like behavior (Extended Data Fig. 4t,u). Altogether, these results demonstrate a specific contribution of developmental *Homer1a/Ania3* to enhancing adult attentional performance. This raises two questions (1) how does endogenous differential expression of short *Homer1/Ania3* isoforms throughout development affect cellular functions underlying attention in the adult, and (2) how do these cellular and molecular changes influence neural dynamics supporting attention?

Low-*Homer1a*-expressing neurons upregulate GABA receptors

To better understand the differences in gene expression programs associated with *Homer1* we performed single-cell RNA-seq (scRNA-seq) from PFC of adult CC083 and CC025 mice (Fig. 5a). After applying quality control filters (Methods) we obtained 70,920 total cells (Extended Data Fig. 5a; 40,897 from CC083 and 30,023 from CC025, $n = 2$ biological replicates per CC line of three mice pooled per replicate). We performed graph-based weighted nearest neighbors clustering analysis and identified major cell types based on cluster-wide expression of several canonical marker genes (Fig. 5b and Extended Data Fig. 5b,c)[40].

As *Homer1* is primarily expressed in neurons[41], we subclustered the neurons (4,633 cells) and re-clustered them based on the first 50 principal components, identifying ten distinct neuronal clusters and their putative cortical layer contributions (Fig. 5c, Extended Data Fig. 5d and Methods). We determined that nine of the clusters were glutamatergic and one was GABAergic based on the expression of marker genes *Slc17a6*, *Slc17a7*, *Slc32a1* and *Gad1* (Fig. 5d). Consistent with previous studies[42,43], *Homer1* expression was primarily restricted to glutamatergic neurons (Fig. 5e). Of the nine glutamatergic clusters, four showed substantial downregulation of *Homer1* in CC083 cells compared to CC025 cells (Fig. 5f; clusters 0, 1, 5 and 6 referred to as *Homer1* DE clusters). To define the gene expression patterns associated with varying levels of *Homer1* we performed differential expression analysis on the *Homer1* DE clusters between CC lines[44]. We then systematically assessed the extent of differential expression of various neurotransmitter and neuromodulatory systems. Notably, we found that CC083 cells uniformly upregulate several GABA receptor subunits and GABA receptor-associated genes, specifically in the *Homer1* DE clusters (Fig. 5g–i and Extended Data Fig. 5e,f), while downregulating several glutamatergic receptor subtypes with almost no differential expression of other neurotransmitter receptors or transporters (Fig. 5g). In further support of this, Gene Ontology analysis of molecular function

Fig. 3 | Chr13 QTL effects map to *Homer1*, but adult manipulations have no behavioral phenotype. a, Schematic of PFC dissection region for RNA-seq in DO high (pink) and low (green) performers. **b**, Volcano plots of differential expression of Chr13 QTL genes between DO high relative to low performers for all locus genes ($n = 3$ per group) from bulk PFC RNA-seq. Dashed lines indicate significance thresholds (Benjamini–Hochberg adjusted $P = 0.05$ and $\log_2$ fold change (FC) = 0.5 or = −0.5, two-sided Wald test). Only *Homer1* crosses both thresholds (red). **c**, Expression levels of *Homer1* isoforms in PFC from DO high and low performers ($n = 3$ per group), significant differential expression of *Homer1a* ($P = 0.0032$) and *Ania3* ($P = 0.0068$) by two-way ANOVA with post hoc Holm–Sidak's test. **d**, Schematic of PFC dissection region for RNA-seq in CC high (CC083, tan) and low (CC025, blue) performers. **e**, Volcano plot showing differential expression of Chr13 QTL genes for CC083 (high performers) relative to CC025 (low performers) mice after DESeq2. Dashed lines indicate significance thresholds (Benjamini–Hochberg adjusted $P = 0.05$ and $\log_2 FC = 0.5$ or = −0.5, two-sided Wald test). Only *Homer1* crosses both thresholds (red). **f**, Expression levels of *Homer1* isoforms in PFC from CC high and low performers ($n = 3$ per group), significant differential expression of *Homer1a* and *Ania3* ($P < 0.0001$ for both) by two-way ANOVA with post hoc Holm–Sidak's test for multiple comparisons. **g**, Schematic of constructs and injection location (PFC) for *Homer1a* knockdown (KD; purple) and control (CTR; Scramble, blue) in adult B6 mice. **h**, Validation histology performed 8 weeks after bilateral injection of AAV-U6-Homer1a shRNA-CMV–mCherry knockdown virus (top) and AAV-U6-Scramble-CMV–mCherry control virus (bottom) into PFC showing viral transduction in the target area (4,6-diamidino-2-phenylindole (DAPI), blue; mCherry, red). Scale bars, 1,000 µm. **i**, *Homer1a* and *Homer1b/c* expression levels (relative to controls) in PFC samples dissected from KD ($n = 3$) and control ($n = 3$) mice measured by qPCR (two-way ANOVA showed significant main effects for shRNA construct, $P = 0.0068$, and *Homer1* isoform expression, $P = 0.0171$, as well as a significant interaction between those variables, $P = 0.0168$; post hoc Holm–Sidak's test for multiple comparisons shows a significant difference in *Homer1a* expression, $P = 0.0031$). **j**, PPI in KD ($n = 14$) and Scramble ($n = 14$) mice measured as percent inhibition at three prepulse intensities: 3, 6 and 12 dB above background (PPI3, 6 and 12, respectively). **k**, Schematic of constructs and injection location (PFC) for overexpression (OE; orange) and control (eYFP, yellow) in adult B6 mice. **l**, Validation histology performed 8 weeks after bilateral injection of AAV-CaMKII(1.3)–eYFP overexpression virus (top) and AAV-CaMKII(1.3)–eYFP control virus (bottom) into PFC, showing viral transduction in the target area (DAPI, blue; eYFP, green). Scale bars, 1,000 µm. **m**, *Homer1a* and *Homer1b/c* expression levels (relative to controls) in PFC samples dissected from OE ($n = 3$) and control eYFP ($n = 3$) mice measured by qPCR (two-way ANOVA showed significant main effects for expression construct, $P = 0.0447$, and *Homer1* isoform expression, $P = 0.0398$; post hoc Holm–Sidak's test for multiple comparisons shows a significant difference in *Homer1a* expression, $P = 0.0282$). **n**, PPI in OE ($n = 9$) and control eYFP ($n = 10$) mice measured as percent inhibition at three prepulse intensities: 3, 6 and 12 dB above background (PPI3, 6 and 12, respectively). Data in **c**,**f**,**i**,**j**,**m**,**n** are expressed as mean ± s.e.m.

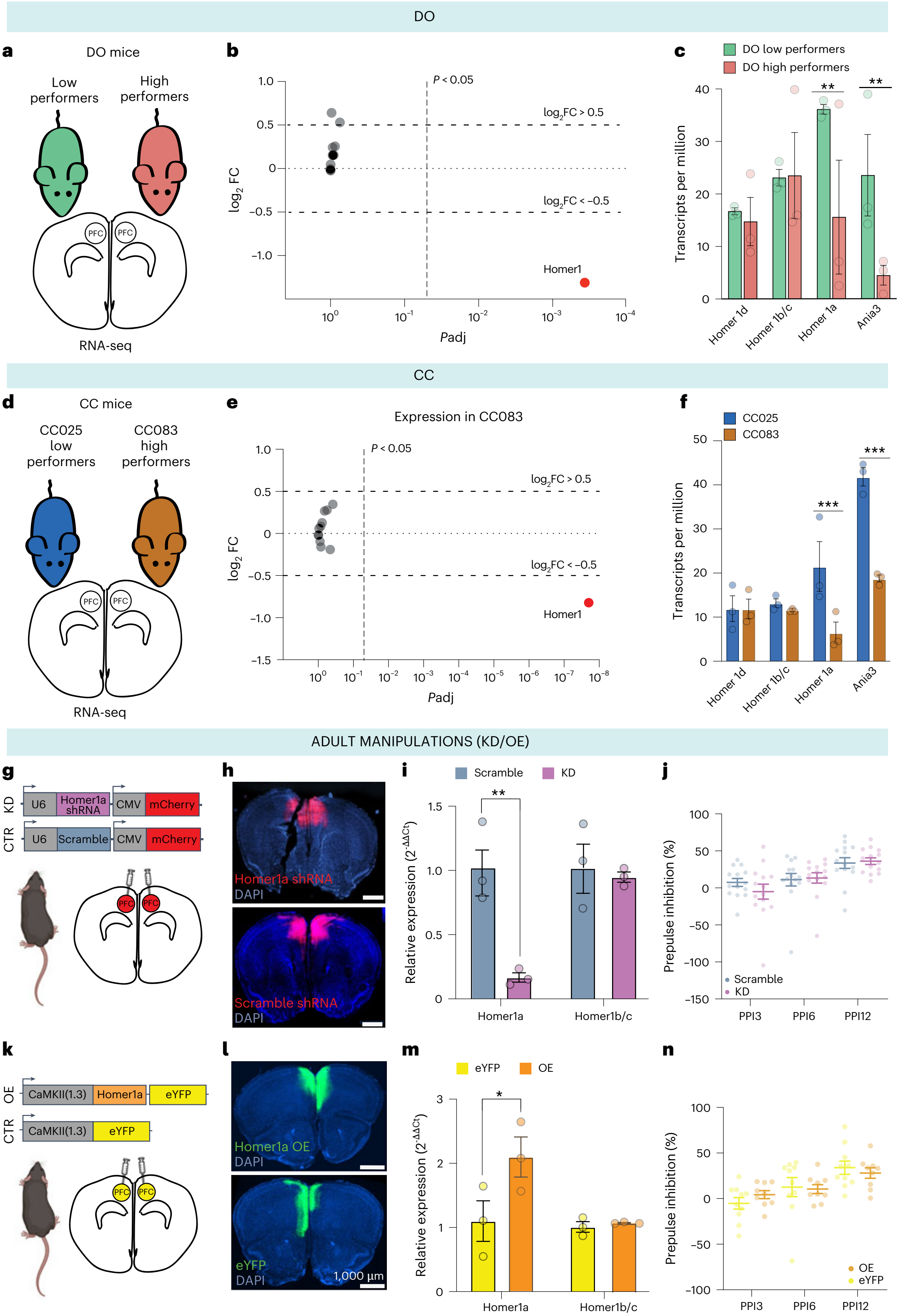
DO
a
DO mice
Low performers
High performers
PFC
PFC
RNA-seq
b
P < 0.05
log$_2$FC > 0.5
log$_2$FC < −0.5
Homer1
log$_2$ FC
1.0
0.5
0
−0.5
−1.0
10^0
10^{-1}
10^{-2}
10^{-3}
10^{-4}
Padj
c
DO low performers
DO high performers
Transcripts per million
40
30
20
10
0
**
**
Homer 1d
Homer 1b/c
Homer 1a
Ania3
CC
d
CC mice
CC025 low performers
CC083 high performers
PFC
PFC
RNA-seq
e
Expression in CC083
P < 0.05
log$_2$FC > 0.5
log$_2$FC < −0.5
Homer1
log$_2$ FC
1.0
0.5
0
−0.5
−1.0
−1.5
10^0
10^{-1}
10^{-2}
10^{-3}
10^{-4}
10^{-5}
10^{-6}
10^{-7}
10^{-8}
Padj
f
CC025
CC083
Transcripts per million
50
40
30
20
10
0
***
***
Homer 1d
Homer 1b/c
Homer 1a
Ania3
ADULT MANIPULATIONS (KD/OE)
g
KD
U6
Homer1a shRNA
CMV
mCherry
CTR
U6
Scramble
CMV
mCherry
PFC
PFC
h
Homer1a shRNA
DAPI
Scramble shRNA
DAPI
i
Scramble
KD
Relative expression ($2^{-\Delta\Delta Ct}$)
1.5
1.0
0.5
0
**
Homer1a
Homer1b/c
j
Prepulse inhibition (%)
100
50
0
−50
−100
−150
Scramble
KD
PPI3
PPI6
PPI12
k
OE
CaMKII(1.3)
Homer1a
eYFP
CTR
CaMKII(1.3)
eYFP
PFC
PFC
l
Homer1a OE
DAPI
eYFP
DAPI
1,000 µm
m
eYFP
OE
Relative expression ($2^{-\Delta\Delta Ct}$)
3
2
1
0
*
Homer1a
Homer1b/c
n
Prepulse inhibition (%)
100
50
0
−50
−100
OE
eYFP
PPI3
PPI6
PPI12

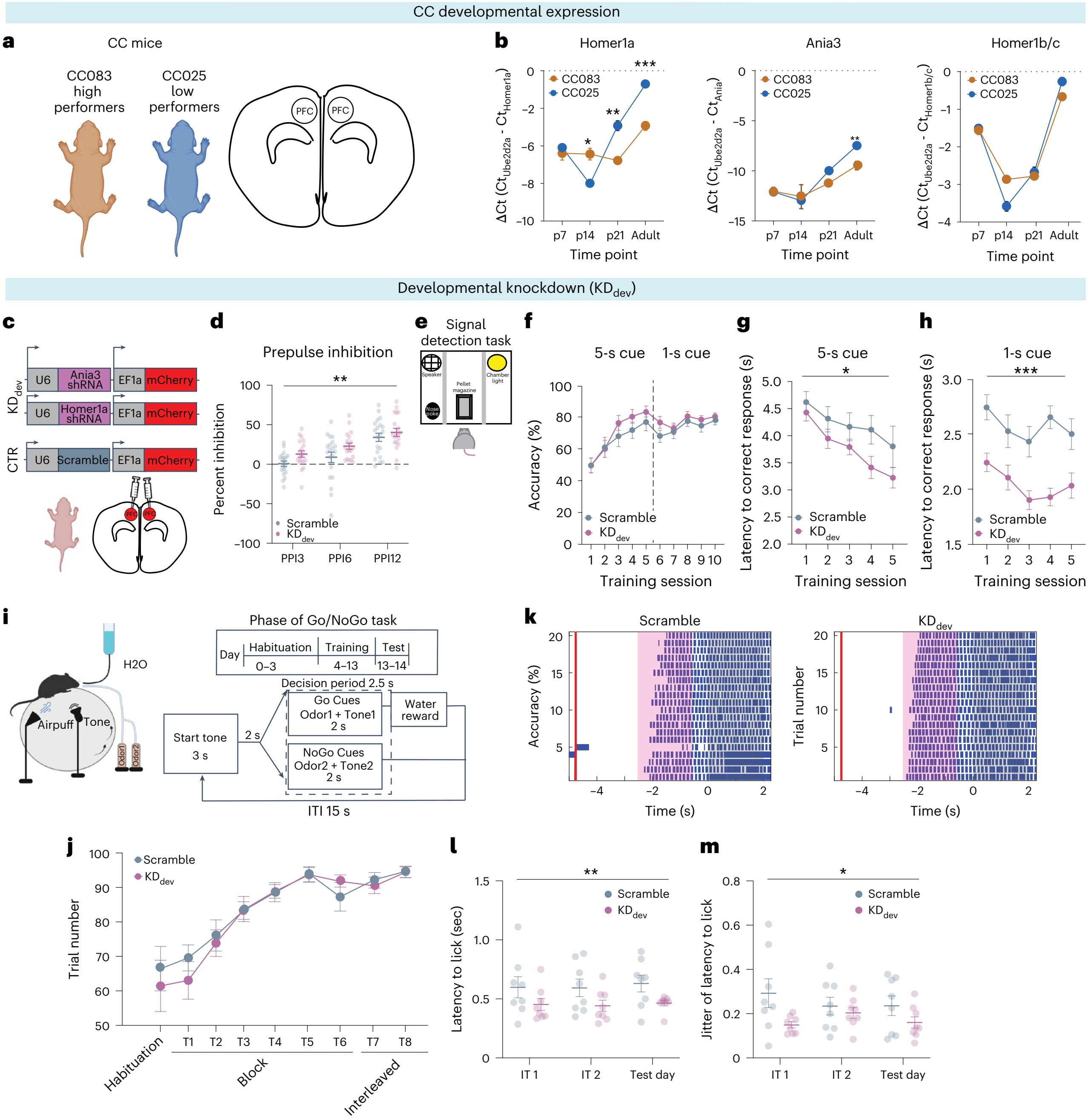

Fig. 4 | *Homer1a* and *Ania3* are developmental modifiers of attention. **a**, Schematic of PFC dissection region in CC high (CC083, tan) and low (CC025, blue) performers for qPCRs across postnatal development. **b**, PFC expression of *Homer1a*, *Ania3* and *Homer1b/c* in CC083 and CC025 mice at p7, p14, p21 and in adult by qPCR ($n = 3$ per strain per timepoint), significant differences for *Homer1a* by two-way ANOVA with post hoc Holm–Sidak's test, $P = 0.0164$ at p14, $P = 0.0021$ at p21 and $P = 0.0004$ at adult; and for *Ania3* $P = 0.0017$ at adult. **c**, Schematic of constructs and injection location (PFC) for KD (KD$_{dev}$, purple) and control (Scramble, blue) in neonatal B6 mice. **d**, PPI in Scramble ($n = 12$ M + 8 F) and KD$_{dev}$, ($n = 11$ M + 8 F). Significant differences between groups by two-way ANOVA ($P = 0.0072$). No significant interaction between sex and group by three-way ANOVA. **e**, Schematic of the operant wall of the arena used for the SDT. **f**–**h**, Performance during SDT across training sessions, shown as accuracy (correct response) percentage (**f**) and mean latency from cue to first response within correct trials for the 5-s cue (**g**, $n = 13$ M + 8 F per group, $P = 0.0354$) and the 1-s cue (**h**, Scramble $n = 9$ M + 6 F; KD$_{dev}$ $n = 11$ M + 7 F, $P < 0.0001$). Significant differences between groups were measured by repeated-measures two-way ANOVA. No significant interactions between sex and group were found by repeated-measures three-way ANOVA. **i**, Schematic of Go/No-Go task setup (left) and training protocol (right). Below is the task structure for interleaved training days testing day. **j**, Go/No-Go task performance accuracy across habituation and training days ($n = 8$ M per group). **k**, Raster plots of licking for the Go/No-Go task for representative Scramble (left) and KD$_{dev}$ (right) mice. Go (right) and No-Go (left) trials were interleaved during testing but are depicted separately. Time 0 is plotted as the end of the decision period. The red bar shows the end of the start tone, pink shading notes the time when cues are delivered, and licks are plotted as blue ticks. **l**, Quantification of the latency to first lick within the decision period of Go trials. Each point is the average latency to first lick for the first ten Go trials per animal ($P = 0.0047$, $n = 8$ M per group, significant main effect between groups by two-way ANOVA). **m**, Quantification of the latency to first lick jitter. Jitter was quantified as the standard deviation of first lick latencies across the first ten Go trials (significant main effect between groups by two-way ANOVA showed a significant main effect between groups, $P = 0.0127$, $n = 8$ M per group). Data in **b**,**d**,**f**–**h**,**j**,**l**,**m** are expressed as mean ± s.e.m.

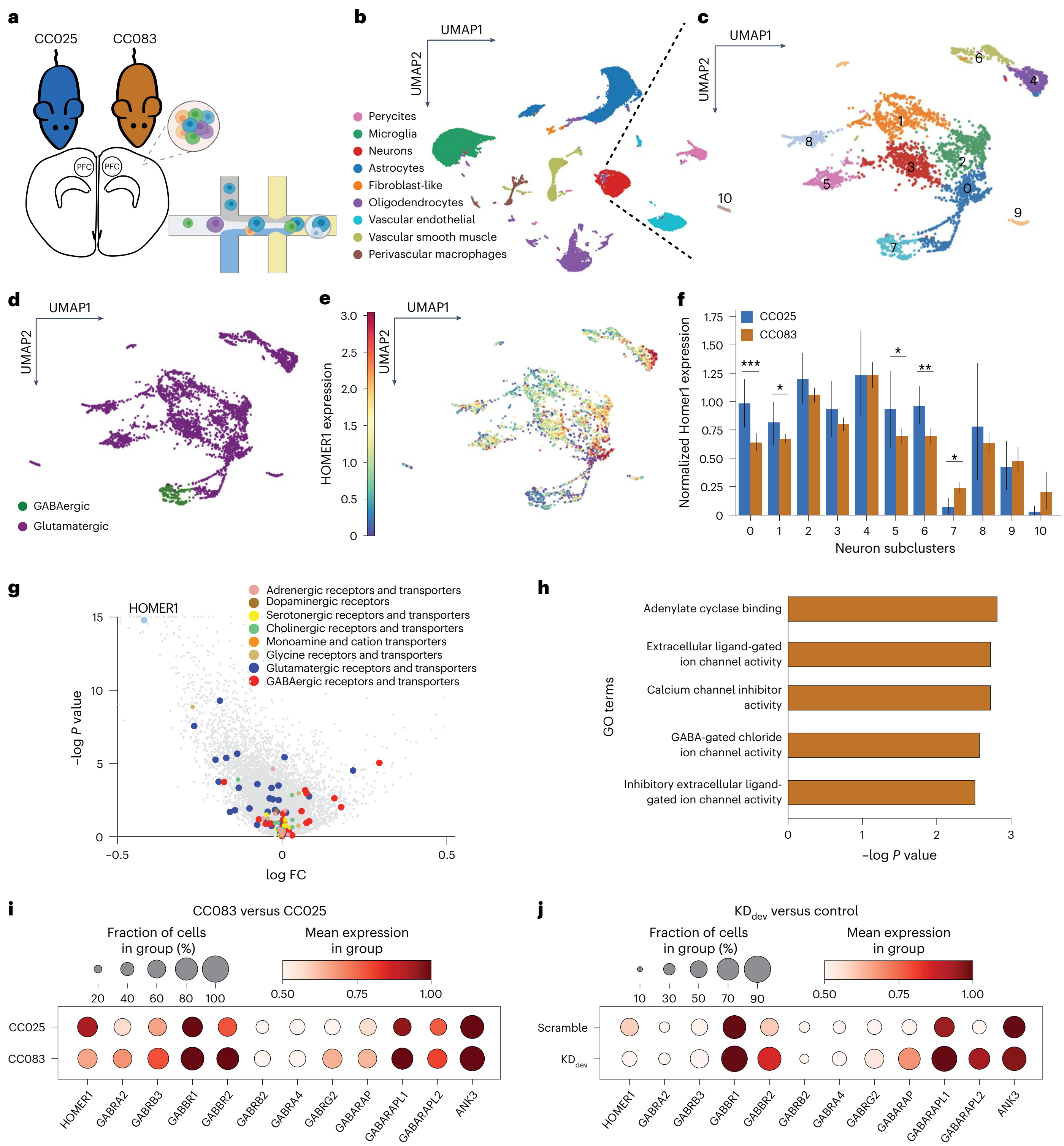

Fig. 5 | Low *Homer1*-expressing glutamatergic neurons upregulate GABA receptors. **a**, Schematic representation of scRNA-seq workflow. **b**, Uniform Manifold Approximation and Projection (UMAP) visualization of all cells collected from CC025 ($n = 6$) and CC083 ($n = 6$) mice clustered based on transcriptional profile. **c**, UMAP visualization subclustering all cells identified as neurons. **d**, Identification of excitatory (glutamatergic) and inhibitory (GABAergic) neuron clusters based on expression of canonical marker genes. **e**, UMAP visualization of scaled *Homer1* expression in neuronal clusters. **f**, Differential *Homer1* expression between CC083 and CC025 neurons by cluster (unpaired *t*-tests, Cluster 0 $P = 0.0004$, Cluster 1 $P = 0.0565$, Cluster 5 $P = 0.0833$, Cluster 6 $P = 0.0048$ and Cluster 7 $P = 0.0215$). Data are shown as mean ± s.d. **g**, Volcano plot depicting differential gene expression in the glutamatergic *Homer1* DE clusters in CC025 and CC083, relative to the CC025. Colored dots indicate genes encoding receptors and transporters of common neurotransmitter systems. **h**, Gene Ontology (GO) analysis of molecular function by Enrichr for genes upregulated in the glutamatergic *Homer1* DE clusters from CC083 mice. Raw *P* values were determined using a one-sided Fisher's exact test. **i**, Dot plots showing scaled expression of GABAergic receptors driving GO analysis (from **h**) in the glutamatergic *Homer1* DE clusters by CC line. **j**, Dot plots showing scaled expression of the same GABAergic receptor genes as in **i** for the glutamatergic cluster in KD$_{dev}$ and Scramble control mice by group. In **i**,**j**, the size of each dot corresponds to the percentage of cells from each group expressing each gene, and the color intensity indicates the relative, scaled expression of that gene.

for genes upregulated in the CC083 cells from the *Homer1* DE clusters showed an enrichment of pathways related to inhibitory GABA signaling (Fig. 5h), whereas CC025 terms overrepresented glutamatergic signaling, driven by GABA and glutamate receptor subunits, respectively (Extended Data Fig. 5g). These data indicate that lower expression of *Homer1* in a subset of prefrontal excitatory neurons yields enhanced GABAergic to glutamatergic receptor balance in those same neurons, suggesting enhanced inhibitory receptivity.

We also assessed the transcriptional programs of upstream GABAergic neurons. We performed differential expression analysis on the GABAergic cluster, in which, notably, *Homer1* is significantly upregulated in the CC083s (Fig. 5f; cluster 7, $P = 0.02$). Due to the well-studied contributions of neuromodulation in attentional processing[45], we assessed expression differences of markers for the most common neuromodulatory systems and found that CC083 GABAergic neurons had higher expression of genes associated with adrenergic and cholinergic signaling than the CC025s (Extended Data Fig. 5i). Furthermore, pathway enrichment analysis[46] indicates a significant overrepresentation of genes related to noradrenergic signaling in CC083s (Extended Data Fig. 5h). Given its historical significance in attentional regulation[47], as well as its role as a target of medications to treat ADHD[48,49], we further analyzed the expression of adrenergic receptors. We found that the higher expression of adrenergic marker genes in CC083 GABAergic cells is driven primarily by the adrenergic receptor *Adra1b*, which seems to be preferentially expressed in the VIP/TAC2 GABAergic subcluster (Extended Data Fig. 5j–l).

Finally, to determine whether these differences between CC lines were recapitulated by developmental changes in *Homer1a/Ania3* expression rather than the many other differences in the CC genomes than those at or near *Homer1*, we prepared another cohort of mice with bilateral injection of either *Homer1a/Ania3* shRNA or scrambled controls at P0. We then performed scRNA-seq from adult mice and performed similar sets of analyses as with the CC mice. We found that within the one main cluster of excitatory neurons (Extended Data Fig. 5m,n), *Homer1* was significantly downregulated in cells from the KD_{dev} mice (Extended Data Fig. 5o), while indeed in those same cells, many GABA receptor subunit and associated genes were significantly upregulated (Fig. 5j). Notably, both the glutamatergic CC *Homer1* DE and KD_{dev} clusters upregulate the GABA receptor gene set, and in a more similar pattern than would be expected by chance (Extended Data Fig. 5p) Taken together, these data demonstrate that developmental prefrontal *Homer1/Ania3* knockdown leads to enhanced inhibitory signaling and influence in PFC. We next explored the consequences of these effects on neural dynamics in the behaving animal during an attention task.

Developmental reduction of *Homer1/Ania3* enhances prefrontal inhibitory tone and SNR

How do the *Homer1a*-associated molecular changes contribute to changes in neural dynamics underlying attentional control? Is there enhanced inhibitory tone in PFC as predicted from the upregulation of GABAergic receptors, and how might this be linked with neuromodulatory input? To address these questions, we recorded multi-area brain activity in CC083 (low-*Homer1a*, high attention) and CC025 mice (high-*Homer1a*, low attention) as they performed the operant SDT. We injected AAV1/9-GCaMP or JRGECO1a into the locus coeruleus (LC; GCaMP), mediodorsal thalamus (MD; GCaMP) and PFC (JRGECO1a to avoid recording from ipsilateral MD terminals), implanted optical fibers above each region and used a custom dual-color fiber photometry system to record bulk calcium signals from these regions simultaneously in behaving mice (Fig. 6a and Methods). The CC025 mice did not tolerate intracranial implants and therefore could not be used for photometry experiments. In their place, we used B6 mice as 'low performers' as they have comparable *Homer1a* expression and behavioral performance to CC025s (Figs. 1b and 2e and Extended Data Fig. 6a). Multi-area neural activity recordings from a given animal were frame-projected onto a camera sensor, and custom scripts were used to extract timeseries data, regress out motion-related artifacts and align to behavioral data (Methods).

We first analyzed baseline home-cage neural activity patterns in CC083 and B6 mice and noticed substantially depressed PFC activity ($P < 0.001$, Welch-corrected *t*-test) in CC083 mice (Fig. 6b). This supported the strong inhibitory influence we expected from the GABAergic upregulation in CC083 mice (Fig. 5g–j). Furthermore, as mice performed the SDT task, we found that CC083s exhibited large increases in PFC activity before and at cue onset, which were greater on shorter latency correct trials compared to long latency trials and omissions (Fig. 6c; example raw traces from correct and incorrect trials shown). More notably, this cue-related activity rapidly diminished during inter-trial intervals (ITIs) (Fig. 6c). Such dynamic task-related fluctuations (cue versus ITI) in CC083s led to consistently high levels of PFC signal-to-noise ratio (SNR; trial-averaged neural activity in cue versus baseline periods of the task) throughout the task (Fig. 6d). These dynamic task-related fluctuations in PFC activity and enhanced SNR were not observed in B6 mice, which exhibited relatively constant PFC responses throughout all task phases, including ITIs and short and long latency responses (Fig. 6c). We also observed steady increases in LC–PFC functional correlations as the task progressed that mirrored behavioral performance (Extended Data Fig. 6b–d), which together with scRNA-seq data of increased adrenergic Adra1b expression in GABAergic cells, suggested that LC may contribute to prefrontal inhibitory tone and SNR.

Fig. 6 | Developmental reduction of *Homer1a/Ania3* alters prefrontal inhibitory influence, enhances SNR and improves attention. a, Schematic of dual-color, four-region photometry system. Simultaneous 565 nm, 470 nm and 405 nm recordings were taken from PFC (jRGECO, red), MD (GCaMP, green) and LC (GCaMP, green) in B6 (gray) or CC083 (tan) mice. **b**, Average activity during baseline for B6 ($n = 4$) and CC083 ($n = 4$ per strain) in PFC during 1-min recordings (two-sided Welch-corrected *t*-test, $P < 0.0001$). **c**, Representative trace from PFC, *y* axis is *z*-scored df/f and *x* axis is time (s) (top). Brown rectangles indicate cues, orange dotted lines indicate delayed responses and blue dotted lines indicate correct responses. PFC activity in task during the 5 s before cue onset of short (<10 s) and long (≥10 s) latency response trials, respectively, and during the last 5 s of ITIs for trials on all days in B6 ($n = 5$) and CC083 ($n = 4$) mice (two-way ANOVA, followed by two-sided Holm–Sidak's test for multiple comparisons, B6 versus CC083 short latency $P = 0.0002$, ITI $P < 0.0001$; CC083 short latency versus ITI $P < 0.0001$) (bottom). **d**, PFC neuronal SNR ((trial pre-cue maximum − baseline mean)/baseline s.d.) 5 s before cue onset in B6 ($n = 5$) and CC083 ($n = 4$) mice for correct trials on all days (two-sided Welch-corrected *t*-test, $P < 0.0001$). **e**, Schematic of dual-color recordings from PFC excitatory neurons (jRGECO, red) and inhibitory neurons (GCaMP, green) in Scramble and KD_{dev} mice. **f**, Example traces from excitatory (top) and inhibitory (bottom) neurons across three trials in Scramble (left) and KD_{dev} (right) mice. **g**, PFC excitatory activity in task during the 5 s before cue onset of short (<10 s) and long (≥10 s) latency response trials, respectively and during the last 5 s of ITIs for trials on all days in Scramble ($n = 6$) and KD_{dev} ($n = 10$) mice (two-way ANOVA, followed by two-sided Holm–Sidak's test, Scramble versus KD_{dev} short latency $P < 0.0001$, long latency $P = 0.0304$, ITI $P < 0.0001$, KD_{dev} short latency versus ITI $P < 0.0001$). **h**, PFC excitatory neuronal SNR 5 s before cue onset in Scramble ($n = 6$) and KD_{dev} ($n = 10$) mice for correct trials on all days (two-sided Welch-corrected *t*-test, $P = 0.0356$). **i**, Putative model: knockdown of *Homer1* improves SNR by reducing PFC activity during baseline periods of a task (here depicted as ITIs) but dynamically elevating activity during cue-presentations. Reduced *Homer1/Ania3* levels lead to increased GABA receptor expression in excitatory neurons (triangles) and increased inhibitory tone from cortical interneurons (circles) in PFC (either by increasing feed-forward inhibition from LC, or how the excitatory neurons sense ongoing inhibition, or both) during non-attentive baseline periods of a task. When attention is required, incoming excitatory input overrides ongoing inhibition to provide targeted cue-related responses.

https://doi.org/10.1038/s41593-025-02155-2

We found particularly compelling the dynamic task-related fluctuations and enhanced SNR in CC083 mice and wanted to next determine whether these effects were recapitulated by changes in *Homer1* expression. We prepared a new cohort of *Homer1a/Ania3* KD_{dev} and Scramble control mice for photometry. We simultaneously recorded excitatory neurons in PFC using CaMKII-jRGECO and inhibitory neurons in PFC using mDlx-GCaMP as mice performed the operant SDT (Fig. 6e and Extended Data Fig. 6e). The results from these experiments beautifully recaptured the SNR effects that we had observed in CC083 versus B6 mice (Fig. 6c,d,f–h). Specifically, PFC excitatory responses, while similar at baseline (Extended Data Fig. 4g), were substantially higher at cue presentation than during ITI, specifically in KD_{dev} mice compared to controls (Fig. 6f,g and Extended Data Fig. 6h), leading to significant improvements in SNR (Fig. 6h), which was reflected in better task performance (Extended Data Fig. 6f). One notable difference between the CC083s and KD_{dev} mice is that the baseline inhibitory tone in KD_{dev} mice was reflected acutely during the task (during ITIs) whereas more chronic inhibitory tone was observed in the CC083s, which was

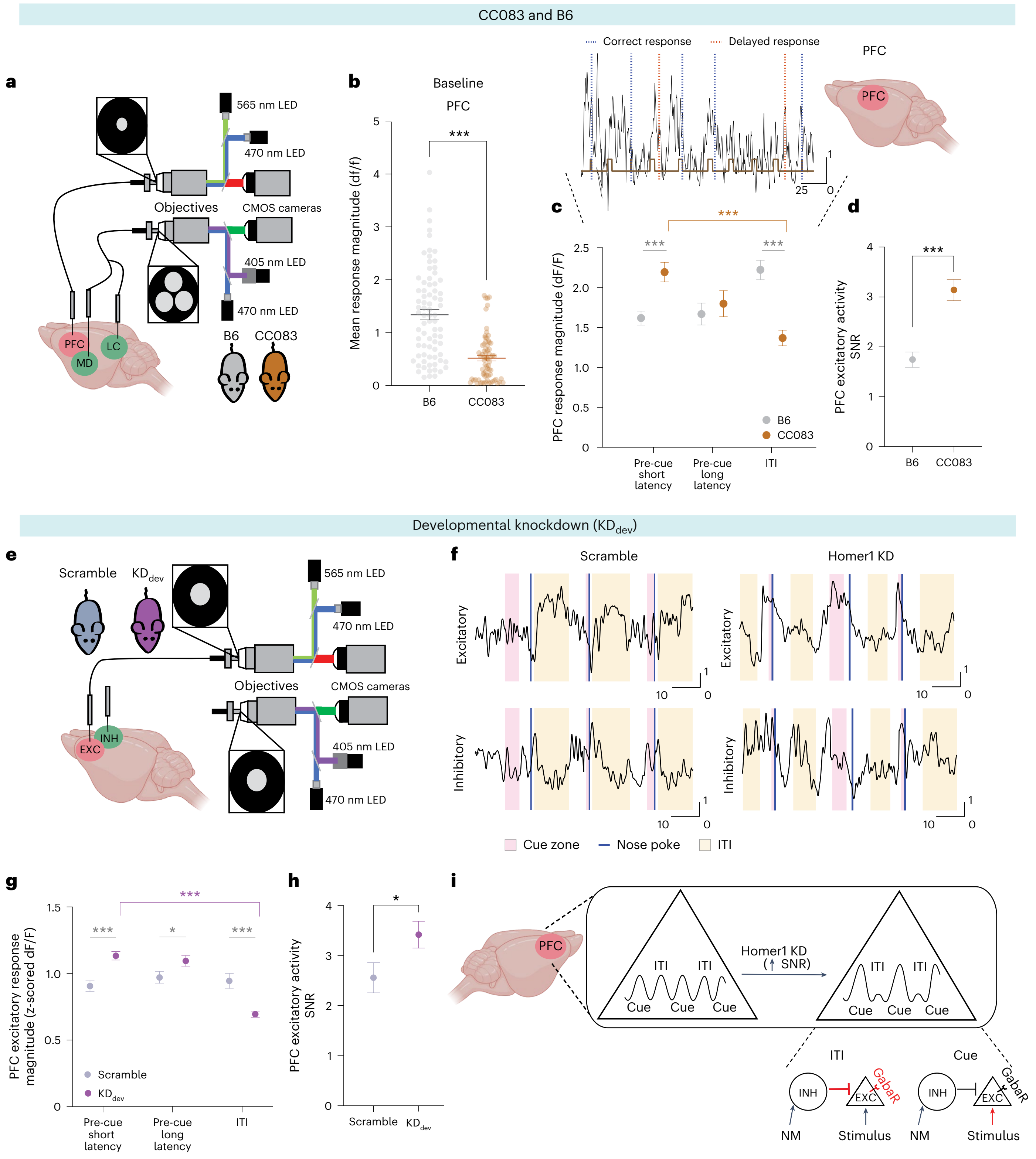

apparent even outside of the task during home-cage recordings (Fig. 6b versus Extended Data Fig. 6g). This may reflect acute compensation of *Homer1* knockdown in KD_{dev} mice or that other effects beyond the locus and gene contribute to a more chronic inhibitory tone in CC083s, which is also reflected in their even higher attentional performance (changes in latency as well as omissions leading to impressive overall increases in task accuracy).

Focusing next on the inhibitory neurons, we found a small but significant increase in the activity of inhibitory neurons during ITIs in KD_{dev} mice compared to controls (Extended Data Fig. 6m), though these were not as striking as the large magnitude changes in excitatory responses during task (Fig. 6g; short-latency cue versus ITI). Thus, *Homer1a/Ania3*-dependent improvements in prefrontal SNR (low activity during ITIs but high at cue presentation) are supported in part by an increase in inhibitory activity (Fig. 6f and Extended Data Fig. 6i,j), but even more so by a greater sensitivity of excitatory neurons to this inhibition (Fig. 6f–h). In sum, these results suggest a model in which low *Homer1a*/*Ania3* increases inhibitory tone, allowing for dynamic scaling of prefrontal activity, and targeted elevations at cue onset, linked to short-latency correct responses (Fig. 6i).

Discussion

Here we performed genetic mapping in outbred mice and identified a short segment on chromosome 13 that is significantly associated with measures of pre-attentive processing. Within this locus, we identified *Homer1*, which encodes a synaptic protein with known roles in regulating excitatory glutamatergic transmission, as a gene that causally affects attentional processing. In particular, knockdown of the short isoforms of *Homer1* (*Homer1a/Ania3*) in prefrontal cortex during a developmental period led to significant improvements in pre-attentive processing and multiple measures of attention in the adult. Notably, the effects of *Homer1a/Ania3* were highly specific to attention, as there were no overall changes in the ability to learn the tasks, and perform other cognitive functions, nor were there obvious sensory-motor impairments or changes in measures of anxiety. We believe the specificity of these behavioral effects on attention is due to the isoform-, region- and developmental-window-specific perturbations of *Homer1/Ania3*. It should be noted that, while *Homer1/Ania3* are often thought of as activity-dependent immediate-early genes[37,50], our findings involve their steady-state expression instead. How variation at the chromosome 13 locus can lead to such targeted cell-type and isoform-specific changes in gene expression of an otherwise ubiquitously expressed gene will be an important avenue of future investigation.

A rich history of work on *Homer1* and its isoforms have revealed important roles in excitatory neurotransmission affecting multiple cognitive domains[51–54], but little is known about its role in attention, particularly by sculpting inhibition and during a defined developmental window. Notably, genes related to *Homer1* signaling have been repeatedly identified in human studies linked to ADHD, suggesting a core underlying gene module for attention[55–58]. In addition to ADHD, *Homer1a* is also associated with schizophrenia[59,60] and autism[61,62], suggesting that early dysfunctions in pre-attentive sensory gating (leading to sensory overload) provide a common etiology driving diverse downstream neuropsychiatric symptoms characterized by hallucinations, hypersensitivity and motor compensations. Thus, prefrontal *Homer1* may be a hub for a deeper mechanistic understanding of pre-attentive processing and attentional control—indeed it has an outsized contribution to the trait and may therefore point us toward unifying circuit models.

In our initial attempts to understand how *Homer1a* might shape behavioral improvements in attentional performance, we explored the molecular programs associated with *Homer1a*-expressing neurons as well as their associated circuit physiology in the context of their inputs and outputs. Through cellular-resolution RNA-seq analysis, we found that low-*Homer1a*, high attention mice (CC083) downregulate *Homer1* expression in a subset of PFC excitatory neurons, which in turn is associated with significant upregulation of GABAergic receptors in these same cells. While the fold expression difference may seem relatively small, it is notable that in comparison with the virtual lack of differential expression in any other neurotransmitter or neuromodulatory system. Moreover, knocking down *Homer1a* locally in PFC during postnatal development led to similar changes in GABAergic receptor upregulation. As GABAergic input can modulate state-dependent SNR[63,64], these findings were accordingly reflected as strong prefrontal inhibitory tone during in vivo neural activity recordings. In both CC083 mice and *Homer1* KD_{dev} mice, we observed suppressed prefrontal activity during baseline periods of the task, but targeted elevations in cue-related activity, enabling short-latency correct choices. Notably, high-*Homer1a*, low-attentional CC performers exhibited uniformly elevated PFC activity at both baseline and cue-related phases of the task. Thus, rather than overall increases in PFC neural activity, a dynamic prefrontal inhibitory influence, increased SNR and targeted cue-specific response enabled attentional performance. Given that widely prescribed medications for ADHD are stimulants acting to elevate PFC activity, which, while effective, can lead to rapid tolerance, a strategy to reduce PFC activity and tune its SNR may be therapeutically promising.

While the current investigations reveal mechanisms of attention related to the interplay of prefrontal inhibitory tone on increased SNR of PFC, an understanding of the more complete effects of *Homer1a* requires deeper investigation. For instance, GABAergic cells from low-*Homer1a* mice upregulate adrenergic and cholinergic signaling that may contribute to feed-forward inhibition and sensory selection, potentially acting over diverse time scales. Furthermore, a deeper cellular resolution investigation of the neural activity in various inhibitory neuron cell types is required to understand how inhibitory tone sculpts the prefrontal microcircuit during attention. Finally, it will be important to understand how *Homer1* influences GABAergic receptor expression and why its effects are more prominent during development. We currently favor a model that posits increased inhibition as a potential compensatory mechanism for reduced Homer1a-mediated homeostatic plasticity[65–67]. Notably, previous studies initiated Homer1a-mediated homeostatic plasticity via $GABA_A$ receptor antagonist treatment, and the induced Homer1a lasted several hours[65,66]. This indicates that (1) GABA signaling is likely a mechanism for maintaining postsynaptic neuronal homeostasis and (2) a homeostatic mechanism involving inhibitory neurotransmission would likely require chronic inhibition to bring the postsynaptic cell to its homeostatic set point. Indeed, we observe marked downregulation of genes involved in inhibitory synaptic homeostasis, such as *NPTX2* and *NPAS4* (refs. 68–70), in the *Homer1* DE cells. Furthermore, implicit in this model is that small changes in inhibition can tightly control SNR. Of note, recent work demonstrated that following sensory overstimulation, young mice exhibited increases in cortical inhibitory input and markers for Homer1a-mediated homeostatic plasticity but older mice did not[71]. Such age-dependent differences in homeostatic plasticity, and extensive previous work on the importance of sensitive periods[72,73], provide a possible rationale for why *Homer1a*/*Ania3*-dependent changes would be required during a circumscribed developmental period to improve attention. In sum, the identification of a single gene with large contributions to attention highlights the importance of prefrontal inhibitory tone in tuning neural SNR and provides tractable inroads into circuit models and therapeutic strategies for attentional processing. More broadly, genetic mapping in DO mice may be a promising approach to dissecting individual behavioral domains that together compose the complex phenotypes of neuropsychiatric disease[74].

Online content

Any methods, additional references, Nature Portfolio reporting summaries, source data, extended data, supplementary information, acknowledgements, peer review information; details of author contributions and competing interests; and statements of data and code availability are available at https://doi.org/10.1038/s41593-025-02155-2.

References

1. Petersen, S. E. & Posner, M. I. The attention system of the human brain: 20 years after. *Annu. Rev. Neurosci.* **35**, 73–89 (2012).
2. Buschman, T. J. & Kastner, S. From behavior to neural dynamics: an integrated theory of attention. *Neuron* **88**, 127–144 (2015).
3. Scheydt, S. et al. Sensory overload: a concept analysis. *Int J. Ment. Health Nurs.* **26**, 110–120 (2017).
4. Chappell, P. B. et al. Guanfacine treatment of comorbid attention-deficit hyperactivity disorder and Tourette's syndrome: preliminary clinical experience. *J. Am. Acad. Child Adolesc. Psychiatry* **34**, 1140–1146 (1995).
5. Konopka, R. J. & Benzer, S. Clock mutants of *Drosophila melanogaster*. *Proc. Natl Acad. Sci. USA* **68**, 2112–2116 (1971).
6. Dudai, Y., Jan, Y. N., Byers, D., Quinn, W. G. & Benzer, S. dunce, a mutant of Drosophila deficient in learning. *Proc. Natl Acad. Sci. USA* **73**, 1684–1688 (1976).
7. Quinn, W. G., Sziber, P. P. & Booker, R. The *Drosophila* memory mutant amnesiac. *Nature* **277**, 212–214 (1979).
8. Vitaterna, M. H. et al. Mutagenesis and mapping of a mouse gene, *Clock*, essential for circadian behavior. *Science* **264**, 719–725 (1994).
9. de Bono, M. & Bargmann, C. I. Natural variation in a neuropeptide Y receptor homolog modifies social behavior and food response in *C. elegans*. *Cell* **94**, 679–689 (1998).
10. McBride, C. S. et al. Evolution of mosquito preference for humans linked to an odorant receptor. *Nature* **515**, 222–227 (2014).
11. Bendesky, A. et al. The genetic basis of parental care evolution in monogamous mice. *Nature* **544**, 434–439 (2017).
12. Hsiao, K. et al. A thalamic orphan receptor drives variability in short-term memory. *Cell* **183**, 522–536.e19 (2020).
13. Chick, J. M. et al. Defining the consequences of genetic variation on a proteome-wide scale. *Nature* **534**, 500–505 (2016).
14. Keele, G. R. et al. Regulation of protein abundance in genetically diverse mouse populations. *Cell Genom.* **1**, 100003 (2021).
15. Saul, M. C., Philip, V. M., Reinholdt, L. G. & Chesler, E. J. High-diversity mouse populations for complex traits. *Trends Genet.* **35**, 501–514 (2019).
16. Valdar, W. et al. Genome-wide genetic association of complex traits in heterogeneous stock mice. *Nat. Genet.* **38**, 879–887 (2006).
17. Parker, C. C. et al. Genome-wide association study of behavioral, physiological and gene expression traits in outbred CFW mice. *Nat. Genet.* **48**, 919–926 (2016).
18. Takahashi, J. S., Pinto, L. H. & Vitaterna, M. H. Forward and reverse genetic approaches to behavior in the mouse. *Science* **264**, 1724–1733 (1994).
19. Blumenthal, T. D. Presidential Address 2014: the more-or-less interrupting effects of the startle response. *Psychophysiology* **52**, 1417–1431 (2015).
20. Geyer, M. A. The family of sensorimotor gating disorders: comorbidities or diagnostic overlaps?. *Neurotox. Res.* **10**, 211–220 (2006).
21. Fendt, M., Li, L. & Yeomans, J. S. Brain stem circuits mediating prepulse inhibition of the startle reflex. *Psychopharmacology* **156**, 216–224 (2001).
22. Vales, K. & Holubova, K. Minireview: animal model of schizophrenia from the perspective of behavioral pharmacology: effect of treatment on cognitive functions. *Neurosci. Lett.* **761**, 136098 (2021).
23. Ellenbroek, B. A. Pre-attentive processing and schizophrenia: animal studies. *Psychopharmacology* **174**, 65–74 (2004).
24. Green, M. F. et al. Perception measurement in clinical trials of schizophrenia: promising paradigms from CNTRICS. *Schizophrenia Bull.* **35**, 163–181 (2009).
25. Swerdlow, N., Geyer, M. & Braff, D. Neural circuit regulation of prepulse inhibition of startle in the rat: current knowledge and future challenges. *Psychopharmacology* **156**, 194–215 (2001).
26. Sobin, C., Kiley-Brabeck, K. & Karayiorgou, M. Associations between prepulse inhibition and executive visual attention in children with the 22q11 deletion syndrome. *Mol. Psychiatry* **10**, 553–562 (2005).
27. Kim, Y., Noh, Y. W., Kim, K. & Kim, E. Hyperactive ACC-MDT pathway suppresses prepulse inhibition in mice. *Schizophrenia Bull.* **47**, 31–43 (2021).
28. Braff, D. L., Geyer, M. A. & Swerdlow, N. R. Human studies of prepulse inhibition of startle: normal subjects, patient groups, and pharmacological studies. *Psychopharmacology* **156**, 234–258 (2001).
29. Ding, Y. et al. Core of sensory gating deficits in first-episode schizophrenia: attention dysfunction. *Front. Psychiatry* **14**, 1160715 (2023).
30. Li, L., Du, Y., Li, N., Wu, X. & Wu, Y. Top-down modulation of prepulse inhibition of the startle reflex in humans and rats. *Neurosci. Biobehav. Rev.* **33**, 1157–1167 (2009).
31. Scholes, K. E. & Martin-Iverson, M. T. Disturbed prepulse inhibition in patients with schizophrenia is consequential to dysfunction of selective attention. *Psychophysiology* **47**, 223–235 (2010).
32. Broman, K. W. et al. R/qtl2: software for mapping quantitative trait loci with high-dimensional data and multiparent populations. *Genetics* **211**, 495–502 (2019).
33. Turner, K. M., Peak, J. & Burne, T. H. J. Measuring attention in rodents: comparison of a modified signal detection task and the 5-choice serial reaction time task. *Front. Behav. Neurosci.* **9**, 370 (2016).
34. Bushnell, P. J. & Strupp, B. J. in *Methods of Behavior Analysis in Neuroscience* (ed. Buccafusco, J. J.) Ch. 7 (CRC Press/Taylor & Francis, 2009).
35. Callahan, P. M. & Terry, A. V. Attention. *Handb. Exp. Pharmacol.* **228**, 161–189 (2015).
36. Bottai, D. et al. Synaptic activity-induced conversion of intronic to exonic sequence in Homer 1 immediate early gene expression. *J. Neurosci.* **22**, 167–175 (2002).
37. Brakeman, P. R. et al. Homer: a protein that selectively binds metabotropic glutamate receptors. *Nature* **386**, 284–288 (1997).
38. Kato, A., Ozawa, F., Saitoh, Y., Hirai, K. & Inokuchi, K. vesl, a gene encoding VASP/Ena family related protein, is upregulated during seizure, long-term potentiation and synaptogenesis. *FEBS Lett.* **412**, 183–189 (1997).
39. Muzzio, I. A. et al. Attention enhances the retrieval and stability of visuospatial and olfactory representations in the dorsal hippocampus. *PLoS Biol.* **7**, e1000140 (2009).
40. Zeisel, A. et al. Molecular architecture of the mouse nervous system. *Cell* **174**, 999–1014.e22 (2018).
41. Shiraishi-Yamaguchi, Y. & Furuichi, T. The Homer family proteins. *Genome Biol.* **8**, 206 (2007).
42. Ango, F. et al. Dendritic and axonal targeting of type 5 metabotropic glutamate receptor is regulated by homer1 proteins and neuronal excitation. *J. Neurosci.* **20**, 8710–8716 (2000).
43. Petralia, R. S. et al. Glutamate receptor targeting in the postsynaptic spine involves mechanisms that are independent of myosin Va. *Eur. J. Neurosci.* **13**, 1722–1732 (2001).
44. Finak, G. et al. MAST: a flexible statistical framework for assessing transcriptional changes and characterizing heterogeneity in single-cell RNA sequencing data. *Genome Biol.* **16**, 278 (2015).
45. Thiele, A. & Bellgrove, M. A. Neuromodulation of attention. *Neuron* **97**, 769–785 (2018).
46. Xie, Z. et al. Gene set knowledge discovery with Enrichr. *Curr. Protoc.* **1**, e90 (2021).

47. Aston-Jones, G. & Cohen, J. D. An integrative theory of locus coeruleus-norepinephrine function: adaptive gain and optimal performance. *Annu. Rev. Neurosci.* **28**, 403–450 (2005).
48. Banaschewski, T., Roessner, V., Dittmann, R. W., Santosh, P. J. & Rothenberger, A. Non-stimulant medications in the treatment of ADHD. *Eur. Child Adolesc. Psychiatry* **13**, I102–I116 (2004).
49. Cinnamon Bidwell, L., Dew, R. E. & Kollins, S. H. α2 adrenergic receptors and attention-deficit/hyperactivity disorder. *Curr. Psychiatry Rep.* **12**, 366–373 (2010).
50. Xiao, B. et al. Homer regulates the association of group 1 metabotropic glutamate receptors with multivalent complexes of Homer-related, synaptic proteins. *Neuron* **21**, 707–716 (1998).
51. Szumlinski, K. K. et al. Behavioral and neurochemical phenotyping of homer1 mutant mice: possible relevance to schizophrenia. *Genes Brain Behav.* **4**, 273–288 (2005).
52. Lominac, K. D. et al. Distinct roles for different homer1 isoforms in behaviors and associated prefrontal cortex function. *J. Neurosci.* **25**, 11586–11594 (2005).
53. Jaubert, P. J. et al. Complex, multimodal behavioral profile of the Homer1 knockout mouse. *Genes Brain Behav.* **6**, 141–154 (2006).
54. Datko, M. C. et al. Behavioral and neurochemical phenotyping of mice incapable of Homer1a induction. *Front. Behav. Neurosci.* **11**, 208 (2017).
55. Elia, J. et al. Genome-wide copy number variation study associates metabotropic glutamate receptor gene networks with attention deficit hyperactivity disorder. *Nat. Genet.* **44**, 78–84 (2012).
56. Sánchez-Mora, C. et al. Epigenetic signature for attention-deficit/hyperactivity disorder: identification of miR-26b-5p, miR-185-5p, and miR-191-5p as potential biomarkers in peripheral blood mononuclear cells. *Neuropsychopharmacology* **44**, 890–897 (2019).
57. Hong, Q. et al. Prefrontal cortex Homer expression in an animal model of attention-deficit/hyperactivity disorder. *J. Neurol. Sci.* **287**, 205–211 (2009).
58. Naaijen, J. et al. Glutamatergic and GABAergic gene sets in attention-deficit/hyperactivity disorder: association to overlapping traits in ADHD and autism. *Transl. Psychiatry* **7**, e999 (2017).
59. Norton, N. et al. Mutation screening of the Homer gene family and association analysis in schizophrenia. *Am. J. Med. Genet. B* **120B**, 18–21 (2003).
60. Spellmann, I. et al. Homer-1 polymorphisms are associated with psychopathology and response to treatment in schizophrenic patients. *J. Psychiatr. Res.* **45**, 234–241 (2011).
61. Kelleher, R. J. 3rd et al. High-throughput sequencing of mGluR signaling pathway genes reveals enrichment of rare variants in autism. *PLoS ONE* **7**, e35003 (2012).
62. Gai, X. et al. Rare structural variation of synapse and neurotransmission genes in autism. *Mol. Psychiatry* **17**, 402–411 (2012).
63. Zhang, S. et al. Long-range and local circuits for top-down modulation of visual cortex processing. *Science* **345**, 660–665 (2014).
64. Batista-Brito, R. et al. Developmental loss of ErbB4 in PV interneurons disrupts state-dependent cortical circuit dynamics. *Mol. Psychiatry* **28**, 3133–3143 (2023).
65. Hu, J.-H. et al. Homeostatic scaling requires group I mGluR activation mediated by Homer1a. *Neuron* **68**, 1128–1142 (2010).
66. Diering, G. H. et al. Homer1a drives homeostatic scaling-down of excitatory synapses during sleep. *Science* **355**, 511–515 (2017).
67. Chokshi, V. et al. Input-specific metaplasticity in the visual cortex requires Homer1a-mediated mGluR5 signaling. *Neuron* **104**, 736–748.e6 (2019).
68. Chang, M. C. et al. Narp regulates homeostatic scaling of excitatory synapses on parvalbumin-expressing interneurons. *Nat. Neurosci.* **13**, 1090–1097 (2010).
69. Bloodgood, B. L., Sharma, N., Browne, H. A., Trepman, A. Z. & Greenberg, M. E. The activity-dependent transcription factor NPAS4 regulates domain-specific inhibition. *Nature* **503**, 121–125 (2013).
70. Spiegel, I. et al. Npas4 regulates excitatory-inhibitory balance within neural circuits through cell-type-specific gene programs. *Cell* **157**, 1216–1229 (2014).
71. Radulescu, C. I. et al. Age-related dysregulation of homeostatic control in neuronal microcircuits. *Nat. Neurosci.* **26**, 2158–2170 (2023).
72. Katz, L. C. & Shatz, C. J. Synaptic activity and the construction of cortical circuits. *Science* **274**, 1133–1138 (1996).
73. Nabel, E. M. et al. Adolescent frontal top-down neurons receive heightened local drive to establish adult attentional behavior in mice. *Nat. Commun.* **11**, 3983 (2020).
74. Nestler, E. J. & Hyman, S. E. Animal models of neuropsychiatric disorders. *Nat. Neurosci.* **13**, 1161–1169 (2010).

Methods

Experimental model and subject details

Animals. C57Bl6/J (B6) and DO (25th generation) male mice were purchased from The Jackson Laboratory. CC male and female mice from the CC002, CC0025, CC035, CC038, CC051 and CC083 lines were purchased from the University of North Carolina at Chapel Hill. Mice were bought at 6–8 weeks old, group housed three to five per cage and kept under a 12-h light–dark cycle in a temperature-controlled environment (70–72 °F) with ad libitum food (PicoLab Rodent diet 20, cat. no. 5053) and water, unless mice were food restricted for behavioral assays. All procedures were conducted in accordance with guidelines approved by the Institutional Animal Care and Use Committees (protocol no. 22087-H) at The Rockefeller University. Number of mice used for each experiment was determined based on expected variance and effect size from previous studies and no statistical method was used to predetermine sample size but our sample sizes are similar to those reported in previous publications[12]. DO phenotyping was performed with all males to sufficiently power the study at affordable cost, but follow-up mechanistic studies involving causal manipulations of *Homer1* were performed in mixed-sex cohorts.

Method details

QTL mapping in diversity outbred mice. *Genotype identification and haplotype reconstruction*. SNP locations and genotypes for the eight founder strains were acquired from ftp.jax.org/MUGA. SNP genotypes for the 182 DO mice were determined using a high-density mouse universal genotyping array, GigaMUGA (GeneSeek). A total of 114,184 SNPs were detected on the 19 autosomes and X chromosomes. Using R/qtl2 (ref. 32), founder haplotype probabilities were reconstructed for all samples and then converted to additive allelic dosages and scaled to 1. Realized genetic relationship matrices, often referred to as kinship matrices, were estimated using the leave-one-chromosome-out (LOCO) method[75], so that the kinship term does not absorb variation explained by the putative QTL. Another QTL mapping software package for multiparental populations, miQTL[76], was used to confirm findings from R/qtl2 and to visualize and assess the level of heterozygosity at the locus of interest.

QTL mapping. Phenotype values from the prepulse inhibition performance were subject to Box–Cox transformation. Then, using R/qtl2, an additive single locus linear mixed model was fit at positions across the genome, producing a genome scan. Potential population structure was controlled for through the inclusion of a random effect to account for correlation structure measured by the kinship matrix. This was performed in R/qtl2 using the LOCO method[75]. For confirmation of the QTL results, we performed a multiple imputation genome scan (11 imputations) using miQTL[76], to assess whether uncertainty in founder haplotype reconstruction was strongly influencing the results. Genome-wide significance thresholds ($\alpha = 0.05$) for the genome scans were determined through 1,000 permutations of the diplotype.

Analysis of founder contributions. To determine the founder haplotype effects driving the Chr13 QTL, we first estimated best linear unbiased predictors, which constrain potentially unstable effects by fitting the QTL term as a random effect. To further confirm these results, we used Diploffect[77], to estimate posterior credible intervals for the haplotype effects as well as the proportion of variance explained by the QTL (sometimes referred to as the locus heritability).

Animal behaviors. *Acoustic startle response and prepulse inhibition*. Acoustic startle response and prepulse inhibition testing was performed as described previously[78]. Startle was measured using a San Diego Instruments SR-Lab Startle Response System. Mice were placed into Plexiglas cylinders resting on a Plexiglas platform with the chamber light on for the entire duration of the experiment. Acoustic stimuli were produced by speakers placed 33 cm above the cylinders. Piezoelectric accelerometers mounted under the cylinders transduced movements of the mice, which were digitized and stored by an interface and computer assembly. Beginning at startle stimulus onset, 65 consecutive 1-ms readings were recorded to obtain the amplitude of the mouse's startle response. For the acoustic startle sessions, the ITI between stimulus presentations averaged on 15 s (range 7–23 s). A 65-dB background was presented continuously throughout the session. Startle pulses were 40 ms in duration, prepulses were 20 ms in duration and prepulses preceded the pulse by 100 ms (onset–onset). The Plexiglas holders were wiped clean and allowed to dry between runs. The acoustic startle sessions consisted of three blocks. Sessions began with a 5-min acclimation period followed by delivery of five startle pulses (120 dB) to allow startle to reach a stable level before specific testing blocks. The next block tested response threshold and included four pulses of five different acoustic stimulus intensities: 80, 90, 100, 110 and 120 dB presented in a pseudorandom order. The third block consisted of 42 trials including 12 startle pulses (120 dB) and ten each of three different prepulse trials (68, 71 and 77 dB preceding a 120-dB pulse) also presented in a pseudorandom order. PPI was calculated as follows using the trials in the third block: 100 − (((average startle of the prepulse + pulse trials)/average startle in the pulse alone trial) × 100). In all experiments, the average startle magnitude over the record window (65 ms) was used for all data analysis. As animals typically exhibit greater values for PPI12 > PPI6 > PPI3, mice exhibiting atypical PPI3 > PPI12 were excluded due to probable hearing impairment. Data points 1.5× the interquartile range above the third quartile or below the first quartile were considered outliers and excluded from analyses.

Signal detection task. Experiments were performed within a Habitest Modular Arena and controlled, recorded, and analyzed by Graphic State 4 software (Colbourn).

Three days before the experiment, mice were gradually food restricted to 85% of their body weight by providing ~2 g of food per mouse per day and habituated to chocolate pellets by providing 2 or 3 pellets per mouse per day in their home cage. From the start of food deprivation and for the entire duration of the experiment, body weight and overall well-being were monitored by daily observation and weighting. All training and testing occurred immediately before daily feeding.

The protocol is divided into multiple phases:

- Magazine shaping. The box is configured to have the chocolate pellet magazine and dispenser, the white LED chamber light and speaker. The mouse enters the box with the chamber light off. A reward pellet is dispensed into the magazine and the light in the magazine goes on at the same time. If the mouse retrieves the pellet, another reward is delivered ~10 s later. Alternatively, if the pellet is not retrieved immediately, the mouse has a variable window of 1–5 min to retrieve the pellet before another is dispensed. The session ends after 20 min. When 75% of the cohort are retrieving ≥15 pellets during the magazine-shaping phase, the experiment moves to the next phase (usually 1–2 days).
- Nosepoke shaping. The box configuration is enriched by the nosepoke port and will stay unchanged until the end of the experiment. The mouse enters the box with chamber light off and is left to explore the box with the new element. Whenever the mouse pokes in the nosepoke port, a reward is dispensed. The session ends when the mouse receives 80 rewards or 20 min has elapsed. When 75% of the cohort is retrieving ≥15 pellets during the nosepoke-shaping phase, the experiment moves to the next phase (usually ~3 days). When quantifying nosepokes, only nosepokes triggering rewards were counted. Nosepoke latencies were quantified as the time from a mouse removing its head from the magazine to the time they next nosepoke. To ensure latencies reflected periods when mice were engaging in the shaping, only latencies <20 s were included.

- SDT, 5-s cue training. The mouse enters the box with the chamber light off. The session begins with an initial pre-cue delay period of the variable duration of 3–5 s. If the mouse pokes during this time, the program moves to anticipatory response contingency (see below). Otherwise, it is followed by an 8-kHz pure tone auditory cue (~71 dB) that lasts for up to 5 s. If the mouse pokes during the cue, the magazine lights up, a chocolate pellet is dispensed and the program moves to ITI contingency (see below). If, on the other hand, the mouse does not poke during the 5-s cue, the cue turns off and the program moves to a post-cue response period that lasts up to 5 s. If the mouse pokes during this phase, the magazine lights up, a chocolate pellet is dispensed and the program moves to ITI contingency. If, on the other hand, the mouse does not poke during the post-cue response period, the program moves to time out contingency (see below). Animals that did not score above 50% were not moved onto the 1-s cue training.
- SDT, 1-s cue training. This phase is exactly the same as the 5-s cue training, with the only exception that the tone (cue) stays on for up to 1 s versus 5 s. The session ends when either the mouse has reached 100 correct responses or 20 min elapses.

ITI contingency: the magazine light turns off, after a 10-s delay, the program returns to the pre-cue delay period. If, on the other hand, the mouse pokes during ITI contingency, the program goes to anticipatory response contingency.

Anticipatory response contingency: the chamber light turns on for 10 s. If the mouse pokes during this time, the program restarts anticipatory response contingency. If, on the other hand, it does not poke, the chamber light turns off and the program moves to the pre-cue delay period.

Time out contingency: the chamber light turns on for 10 s. If the mouse pokes during this time, the program moves to the delayed response contingency. If it does not, the chamber light turns off, the trial is considered omitted and the program moves to the pre-cue delay period.

Delayed response contingency: the chamber light turns on for 10 s. If the mouse pokes during this time, the program restarts the delayed response contingency. If it does not, the chamber light turns off, the trial is considered omitted and the program moves to the pre-cue delay period. The session ends when either the mouse has reached 100 correct responses or 20 min elapses. When 75% of the cohort is getting ≥70% trials rewarded for 2 consecutive days in SDT training 1, the experiment moves to the next phase.

Training sessions were matched across cohorts by days until reaching the criteria and plotted from the first training day where the cohort requiring the fewest training days had an average accuracy above 30% (5-s cue training session 1). Data were normalized across operant boxes and experimental groups within a cohort relative to 5-s cue training session 1. Untethered animals that never had more than 30% accurate responses were excluded from all SDT behavioral analyses. Animals that reached criteria for 5-s cue training but never have more than 50% accuracy in 1-s cue training were excluded from 1-s cue training analyses. Animals that decreased in accuracy by over 20% in consecutive days in a given cue length training phase were excluded from that phase's analyses.

Auditory brainstem recording thresholds. The mice were anesthetized with ketamine (110 mg kg^{-1}) and xylazine (11 mg kg^{-1}) via intraperitoneal injection before all procedures. Once a suitable plane of anesthesia was reached, 1 ml of chilled 0.9% sodium chloride was subcutaneously injected into the mouse's back for hydration. Eyes were moistened with ophthalmic ointment (Puralube, Dechra Veterinary Products). The anesthetized animal was then placed in a sound-isolated, electrically shielded box on top of a heating pad (40-90-2-05, FHC). A rectal probe and DC temperature controller (41-90-8D, FHC) were used to maintain the mouse's temperature near 38 °C. Needle electrodes (GRD-SAF, The Electrode Store) were subdermally placed behind the pinna of the tested ear (reference electrode), in the scalp between the ears (active electrode) and in the back near the tail (ground electrode). ABRs were evoked by tone bursts of 4, 8, 16 and 32 kHz produced by a closed-field magnetic speaker connected to a power amplifier (MF1 and SA1, Tucker-Davis Technologies). Each 5-ms burst was presented 33.3 times per second with alternating polarity. The onset and offset of each burst was tapered with a squared cosine function. For each frequency, the sound pressure level was lowered from 80 dB SPL in 5–10-dB steps until the threshold was reached. If 80-dB SPL was not enough to elicit a response, higher intensities were produced. The entire sound delivery system was calibrated with a 0.25-inch condenser microphone (4939-A-011 and 2690-A-0S1, Brüel and Kjær). The electrical response evoked by the tone bursts and measured by the needle electrodes was amplified 10,000 times and bandpass filtered at 0.3–3 kHz (P55, Astro-Med). The amplified response was then digitally sampled at 10-µs intervals with a data-acquisition device (PCI-6259, National Instruments) controlled by custom software (LabVIEW 2019, National Instruments). The electrical responses to 1,000 bursts were averaged at each intensity level to determine the threshold, which was defined as the lowest level at which any response peak was distinctly and reproducibly present. Visual inspection of the vertically stacked responses facilitated threshold determination.

Rotarod. On day 1 (habituation), mice were placed on a rod moving at a constant speed of 4 rpm for 5 min. On day 2, mice were placed on the rod that was moving with an accelerating speed from (4–40 rpm over the 5-min trial), for four consecutive trials. The latency (s) to fall from the rod was measured by an experimenter for each trial, then averaged across trials and used as a measure of motor coordination. The cutoff time was 300 s.

Spontaneous alternation. Tests consisted of a single 5-min trial, in which the mouse was allowed to explore all three arms of a Y-maze (12 × 3 × 5 inch (L × W × H)), while being recorded using a ceiling-mounted camera under red light illumination. Mice were acclimated to the experimental site for 1 h before all experiments. The experimenter was blind to the viral condition of all mice during behavioral testing, with the exception of CC083 versus CC025 tests due to the difference in their coat color. The animal behavior was automatically tracked and analyzed by the EthoVision XT (Noldus) software for (1) total number of entries into each arm, (2) sequences of arm entries and (3) distance moved (inches). Correct alternation (% of total number of arm entries) was defined as consecutive entries in three different arms. Total number of entries into each arm as well as total distance moved in the apparatus served as controls to exclude confounding factors to the memory performance, such as arm bias and/or differences in gross motor activity. Animals 1.5× the interquartile range above the third quartile or below the first quartile were considered outliers and excluded from analyses.

Open field. Thigmotaxis was determined in an open field box (16 × 16 × 16 inch), virtually divided in a peripheral and a central zone 50% smaller. Each mouse was allowed to explore the apparatus for 15 min and its behavior was recorded by a camera and analyzed by EthoVision. The time spent by the animal in the center of the arena was measured. In this test, the preferential exploration of the peripheral zone of the open field is considered an index of anxiety. Animals 1.5× the interquartile range above the third quartile or below the first quartile were considered outliers and excluded from analyses.

Elevated plus maze. This test is commonly used to evaluate anxiety-like behavior in rodents[79]. The apparatus was composed of four black plastic arms, arranged as a cross, located 55 cm above the plane of a laboratory bench and illuminated by a 60 W lamp located above the apparatus. Two closed arms, opposite to each other, were enclosed by lateral walls (50 × 6 × 40 cm), whereas the other two open arms were without walls (50 × 6 × 0.75 cm); the closed and open arms delimited a small square (6 × 6 cm) called the center. Each mouse was placed into the center of the maze, facing one of the two open arms and its behavior was video-recorded for 5 min and automatically analyzed by the EthoVision XT software (Noldus) for the time spent by the mice in each of the three compartments (open, closed and center), which was measured by an observer blind to the experimental groups. Animals 1.5× the interquartile range above the third quartile or below the first quartile were considered outliers and excluded from analyses.

Three-chamber social interaction. Tests used an 18 × 18 × 12 inch (L × W × H) clear acrylic arena, which was divided into three chambers of equal area (18 × 6 × 12 inch; L × W × H) that were separated by walls 6-inches in length on each side, so that there was a 6-inch-long separation in each wall that a mouse could pass through. Mice were habituated to the testing area for 1 h before the start for the experiment. The test began with a 5-min habituation phase to the center chamber, in which the openings in the walls were obstructed so that the mice could not see or enter either opening. Mice were then put in a transfer cage for 1 min as the center walls were opened, after which the mice were returned to the center chamber for a 5 min habituation phase to all three chambers of the arena. Mice were then returned to the transfer cage for 5 min and the arena as wiped down with 10% ethanol, and wire cups were placed upside down in the center of the outer two chambers either with a nonsocial stimulus (foam figurine) or a novel, age- and strain-matched mouse underneath. Mice were then placed back in the center chamber and allowed to explore for 15 min. Behavior was video-recorded and automatically analyzed by the EthoVision XT software (Noldus) for time spent in each chamber and time spent exploring a 3-cm proximity to the social or the nonsocial stimuli (social and nonsocial zones, respectively). The social discrimination index was calculated as the difference between the mouse's time in the social zone and the nonsocial zone, divided by the total time exploring both zones.

Go/No-Go behavior. Mice were head-fixed in place above the center Styrofoam ball (axially fixed with a rod passing through the center of the ball and resting on post holders) and allowed to move freely forward and backward. MATLAB engine ViRMEn was used to design the virtual task landscape and a National Instruments Data Acquisition (NIDAQ) device provided transistor–transistor logic (TTL) pulses to trigger the Arduino Unos controlling the tones, odors, air puff and lick port. Capacitance changes of the lick port during licking were also recorded through the NIDAQ device.

Before behavioral training (2–3 days), the home cage water was replaced with water containing 1% citric acid to increase motivation to receive water rewards throughout the task. Habituation began with mice receiving water rewards during Go cues presentation (odor, isoamyl acetate; pure tone, 6 kHz). After 3–4 days, mice were trained using blocks of Go and No-Go cue (odor, lavender oil; pure tone, 1 kHz) trials. Delivery of water rewards required mice to lick during Go cue presentation and an aversive air-puff punishment (25 psi) was delivered to the flank of the mouse for licking during No-Go cues. After mice completed the block trials with 70% or greater accuracy, Go and No-Go trials were pseudo-randomly interleaved (60–80 trials in total).

$$\begin{aligned}\text{Accuracy} = {} & (\text{no. correctly selected Go trials} \\ & +\text{no. correctly rejected No} - \text{Go trials})/\text{total trials}\end{aligned}$$

Mice completing the trials with 70% or greater accuracy for two consecutive days would then move on to testing. The testing trial structure was as follows: a 2-s trial start tone (pure tone, 3 kHz) began each trial followed by a 2-s delay, then either Go or No-Go cues were presented (2-s presentation). At the onset of the cue presentation a decision window began and lasted for 2.5 s. A correct selection of the Go cues was made by licking within this decision window and a water reward was delivered at the end of correctly identified decision periods. Correct rejections of No-Go cues were measured by the absence of licking within the decision window. Each trial was followed by a 15-s ITI.

Head-fixed signal detection behavior. Following the completion of Go/No-Go testing, mice were tested on the SDT. Each trial began with a 2-s trial start tone (pure tone, 3 kHz) and following a 2-s delay, mice were presented with increasingly shortened Go cues (odor, isoamyl acetate; pure tone, 6 kHz; cue length: 2 s, 1 s and 0.5 s). After the Go cue presentation began, a decision window of 2.5 s opened and mice that licked within this window received a water reward.

Attentional set shift. One week before the test day, mice started a food deprivation protocol to achieve 80–85% of the initial weight. On day 1 and in each consecutive day, they were handled, weighed and fed ~20 g of food pellet and a few chocolate pellets (Bio-Serv). On the day of the experiment, the mice were introduced to a square open field arena (16 × 16 × 16 inch) for five consecutive trials and their behavior was recorded by a camera and analyzed by EthoVision XT (Noldus) software, similar to previous studies[39]. Each of the arena walls had a different visual cue, and in front of each of them, on the floor and ~3 inches from the wall, there was a medicinal cup containing bedding mixed with either sage, cinnamon, cumin or cloves (2 g of spice in 500 g bedding). During the pretrial (T0), the mice were introduced to the arena for 5 min and allowed to explore the cups. This phase was necessary to assess the mice exploratory activity and exclude any odor bias, as well as differences between groups in sensitivity to the odors. For each of the successive four trials (T1–T4), the mice were re-introduced to the arena for 5 min, and the cup containing sage was enriched by adding a chocolate pellet (reward). From trial to trial, the cups position was randomly shifted so that the odor–visual cue pair was always different, but it was kept fixed for all mice. To correctly perform the task, the mice must learn to ignore the visual cue that remains at a fixed location and selectively pay attention to the odor as they change position in the maze from trial to trial. During ITI, the mice were moved to a holding cage while the experimenter cleaned the arena with 10% ethanol, replaced the cups with clean ones and re-baited the sage cup. The exploration time spent by the mice on each cup was recorded, as well as the latency to reach the correct cup (sage) and retrieve the pellet. Mice that did not locate the chocolate pellet in the initial 3 min of trial 1 were excluded from the analysis.

Novel object recognition task. This test began with 2 days of habituation where the mice were allowed to explore an empty square arena (16 × 16 × 14 inch; L × W × H) for 15 min. During training (day 3), mice were re-introduced to the arena, where two identical objects were positioned in the back left and right corners of the cage. Each animal was placed in the middle point of the wall opposite the objects and allowed to explore them for 15 min. At the end of the training phase, mice returned to their home cage for 15 min, while the box and the objects were cleaned with 10% ethanol and then water. Successively, the mice re-entered the arena for the test, during which, one of the two (familiar) objects was replaced with a new one (novel), totally different in color, texture and shape. Each mouse was left to explore freely the objects for 5 min. The entire experiment was recorded using a ceiling-mounted camera and the animal behavior was automatically tracked and analyzed by the EthoVision XT (Noldus) software. Two measures were considered (1) total exploration time (s) spent by the animal interacting with the two familiar objects during training, to evaluate object bias and (2) the exploration time spent by the animal interacting with the novel object over total exploration time (for example, (novel/(familiar + novel)) × 100) during the test. Object exploration time was defined as the time during which the mouse nose was in contact with the object or directed toward it at a distance ≤2 cm.

RNA expression analysis. *RNA extraction from brain tissues*. For tissue extraction, p28 and adult (up to p120) mice were killed by cervical dislocation and immediately decapitated, whereas p7, p14 and p21 mice were killed by decapitation in compliance with Institutional Animal Care and Use Committee protocol no. 22087-H. The targeted brain regions were collected from 1-mm brain slices, obtained by brain matrices (ZIVIC) using 1.0-mm tissue punches and transferred to a tube containing 300 µl of ice-cold lysis buffer and 3 µl β-mercaptoethanol (Total RNA Purification kit, NORGEN; following the manufacturer's protocol). Samples were then homogenized by passing a 25G insulin syringe six times and left on ice. For RNA extraction, the Total RNA Purification kit was used according to the manufacturer's instructions (NORGEN). RNA quality was evaluated by a Bioanalyzer 2100 (Eukaryote Total RNA Nano chip, Agilent) at the Rockefeller University Genomic Resource Center (RIN ≥ 7.50 and free of genomic DNA contamination). RNA samples were then aliquoted and stored at −80 °C.

Bulk RNA sequencing and analysis. For RNA-seq, RNA libraries were prepared from 100 ng of total RNA per sample for six DO mice that were chosen based on upper and lower quartile behavioral effects and also having the appropriate 'high' and 'low' haplotype contribution at the identified QTL, three brain regions per mouse using the TruSeq stranded mRNA LT kit (cat. no. RS-122-2101, Illumina). These libraries cover a range of concentrations, lengths and GC content and were validated for the quantity and fidelity using a TapeStation (Agilent) before downstream procedures. Libraries prepared with unique barcodes were pooled at equal molar ratios following the manufacturer's protocol (cat. no. 15035786 v.02, Illumina). The pool was denatured and subject to paired-end 50 (DO samples) or single-end 100 (CC samples) sequencing on the NovaSeq SP platform. An average of 67 million reads per sample were obtained. Sequencing reads were aligned to the mouse genome (mm10) using STAR[80] (v.2.4.2a) and aligned reads were quantified using Salmon[81] (v.0.8.2). Approximately 90% of the reads mapped uniquely. Hierarchical clustering and principal-component analysis were performed following Variance Stabilizing Transformation (VST) from DESeq2 (ref. 82), which is on the $\log_2$ scale and accounts for library size differences. The hierarchical clustering heatmap shows the Euclidean distances of VST of the counts between samples.

Quantitative PCR. For qPCR, each reverse transcription was performed with 200 µg RNA using the High-Capacity RNA-to-cDNA kit (Applied Biosystems, 4387406), in a final volume of 20 µl. Primers for reverse transcription were equal mixtures of poly-T nucleotides and random hexamers. Negative controls (omitting reverse transcriptase enzyme) were performed for each sample. The complementary DNA products were diluted 1:1 and 2 µl was analyzed by qPCR using custom primer sets and PowerUp SYBR Green Master Mix (10 µl total reaction, Applied Biosystems, cat. no. A25742). Quantitative PCR with reverse transcription (RT-qPCR) was performed using QuantStudio3 (Applied Biosystems) or LightCycler 480 (Roche). Every reaction was systematically run in triplicate. Conditions were 50 °C for 2 min, 95 °C for 10 min, then 40× (95 °C for 15 s and 60 °C for 1 min). qPCR Ct values were analyzed using the QuantStudio or LightCycler software. Detection threshold was set at DRn of 0.3, with this limit always within the 2n exponential amplification phase of genes. The mean of technical triplicate values was reported. All mice gene expression Ct values were normalized with the reference gene Ube2d2a using dCt method to determine the relative mRNA expression of each gene. Developmental knockdown mice that expressed both *Homer1a* and *Ania3* at levels higher than the average Scramble expression by half a standard deviation or more were post hoc excluded from downstream analyses.

The qPCR primers were designed using the Primer3 software and validated for specificity using Primer-BLAST. The following primer sequences were used for qPCR assays:

Homer1a: forward: 5′- CTGACCAGTACCCCTTCACAG; reverse: 5′- CCACCTTACTTAATCATGATTGCTGA
Ania3: forward: 5′- AGCCAACTCAGAATGCATTGCCA; reverse: 5′- AACCAAGGCCAGAGGAGCTCTC
Homer1b/c: forward: 5′- AGCTGAACCAGACAGTGCAGGA; reverse: 5′- CCTCTGTTCTTGGAGTTCTCTGGCA
Ube2d2a: forward: 5′- CAGTGTTTCATTGGCAGGCT; reverse: 5′- GGCGGTTTGAAGGGGTAATC

Gene expression manipulation experiments in vitro and in vivo. We used the following shRNAs for gene knockdown (which were then subcloned into a pscAV-U6–mCherry construct, VectorBuilder/Vector Biolabs):

Homer1a (GenBank NM_011982.4), targeting sequence GGTTTCAGAAACTCTTGAA; *Ania3* (GenBank NM_001347598.1), targeting sequences GGAGACATAGTTCTTCTTA and GCTAAGCTAGAGCCATCTA.

Targeting sequences were selected using the Thermo Fisher BLOCK-iT Designer and the BiOSETTIA shRNA Designer.

For gene expression, the coding sequences of *Homer1a* and *Ania3* were cloned from mouse cortical cDNA and subsequently subcloned into a pAAV.CamKII(1.3).eYFP.WPRE.hGH expression vector using standard molecular cloning techniques. Constructs were verified first by Sanger sequencing, and then diagnostics for inverted terminal repeat sequence integrity, by digestion with SmaI, before AAV production.

Surgical procedures. Surgical procedures and viral injections were carried out under protocols approved by Rockefeller University Institutional Animal Care and Use Committee and were performed in mice anesthetized with 1–2% isoflurane using a stereotactic apparatus (Kopf) under a heating pad. Paralube vet ointment was applied on the eyes to prevent drying.

Viral injections. Virus was injected using a 34–35G beveled needle in a 10 µl NanoFil Sub-Microliter Injection syringe (World Precision Instruments) controlled by an injection pump (Harvard Apparatus). All viruses were injected at a volume of 1 µl and a rate of 100 nl min^{-1} (unless otherwise mentioned), and the needle was removed 10 min after the injection was completed to prevent backflow of the virus. All injection coordinates were relative to bregma.

For adult knockdown manipulations, B6 mice were bilaterally injected at the age of 8 weeks in the PFC (anterior–posterior (A/P) 1.8 mm, mediolateral (M/L) ±0.3 mm, dorsoventral (D/V) −1.75 mm) with an scAAV9 expressing either a U6-Scramble (nontargeting) shRNA-CMV–mCherry (titer 9.87×10^{12} GC per ml, VectorBuilder) or U6-Homer1a-targeted shRNA-CMV–mCherry (titer 4.8×10^{12} GC per ml, VectorBuilder) construct.

For adult overexpression manipulations, B6 mice were bilaterally injected (two injections per hemisphere) at the age of 8 weeks in the PFC (A/P 1.8 mm, M/L1 ±0.3 mm, M/L2 ±0.45 mm, D/V −1.75 mm) with an AAV9 expressing either CaMKII(1.3)-eYFP (titer = 1.0×10^{13} GC per ml) or CaMKII(1.3)-Homer1a-eYFP (titer = 1.0×10^{13} GC per ml) construct at a volume 0.5 µl for each injection. pAAV.CamKII(1.3).eYFP.WPRE.hGH was a gift from K. Deisseroth (Addgene plasmid #105622; http://n2t.net/addgene:105622; RRID:Addgene_105622).

For developmental knockdown experiments, injections in pups were performed according to previously described anesthesia and injection protocols[83]. Here, B6 pups were bilaterally injected in PFC at p0 (A/P ~0.3 mm, M/L ~±0.15–0.2 mm, D/V ~−0.7–0.8 mm) with an AAV9 expressing either a U6-Scramble (nontargeting) shRNA-EF1a–mCherry (titer = 4.8×10^{12} GC per ml) or pooled U6-Homer1a-targeted shRNA-EF1a–mCherry and U6-Ania3-targeted shRNA-EF1a–mCherry construct (titer = 2.8×10^{12} GC per ml, Vector Biolabs) construct at a volume of 0.1 µl both times. This age was selected to allow sufficient time for the viruses to express by the targeted developmental window (p14–p21) based on observations from the CC (Fig. 4b). These mice began behavioral testing between 8 and 12 weeks of age.

For multifiber photometry experiments, a mixture of AAV9-CaMKII(0.4)-Cre (titer 1.0×10^{13}) and AAV1-Cag-Flex-JRGECO1a (titer 1.0×10^{13}) was injected into PFC (A/P 1.85 mm, M/L 0.35 mm, D/V −2.55 mm) at a combined volume of 1 µl. AAV9-Syn-GCaMP6f (titer 1.4×10^{13} GC per ml) was injected ipsilaterally into MD (A/P −1.6 mm, M/L 0.45 mm, D/V −3.2 mm). AAV(Olig001)-MAG-GCaMP6f (titer 1×10^{13} GC per ml, Univ. Arizona Viral Production Core) was injected into PFC contralaterally (coordinates A/P 1.85 mm, M/L −0.35 mm, D/V −2.55 mm). AAV1-Cag-GCaMP6f (titer 2.6×10^{12}) was also injected contralaterally to the initial injection (Cag-Flex-JRGECO1a) into LC (A/P −5.4 mm, M/L −0.85 mm, D/V −3.6 mm). pENN.AAV.CamKII 0.4.Cre.SV40 was a gift from J. M. Wilson (Addgene viral prep #105558-AAV9; http://n2t.net/addgene:105558; RRID:Addgene_105558), pAAV.CAG.Flex.NES-jRGECO1a.WPRE.SV40 was a gift from D. Kim and the GENIE Project (Addgene viral prep #100852-AAV1; http://n2t.net/addgene:100852; RRID:Addgene_100852;)[84], pAAV.Syn.GCaMP6f.WPRE.SV40 was a gift from D. Kim and the GENIE Project (Addgene viral prep #100837-AAV9; http://n2t.net/addgene:100837; RRID:Addgene_100837), pAAV.CAG.GCaMP6f.WPRE.SV40 was a gift from D. Kim and the GENIE Project (Addgene viral prep #100836-AAV1; http://n2t.net/addgene:100836; RRID:Addgene_100836)[85], Olig001 was a gift from T. McCown (Addgene plasmid #170716; http://n2t.net/addgene:170716; RRID:Addgene_170716)[86].

Cannula implants. Immediately following viral injections, mice undergoing photometry experiments were implanted with 1.25-mm ferrule-coupled optical fibers (0.48 NA, 400-µm diameter, Doric Lenses) cut to the desired length so that the implantation site was ~0.2 mm dorsal to the injection site. Cannula implants were slowly lowered using a stereotaxic cannula holder (Doric) at a rate of 1 mm min^{-1} until it reached the implantation site, 0.2 mm dorsal to the injection site. Optic glue (Edmund Optics) was then used to seal the skull–cannula interface and a custom titanium headplate was glued to the skull using adhesive cement (Metabond).

Mice recovered for 5 weeks after *Homer1* manipulations and 3 weeks after photometry implants before experiments began.

Histology and immunohistochemistry. Mice were transcardially perfused with PBS and 4% paraformaldehyde in 0.1 M phosphate buffer, then brains were post-fixed by immersion for 24 h in the perfusate solution followed by 30% sucrose in 0.1 M phosphate buffer at 4 °C. The fixed tissue was cut into 40-mm coronal sections using a freezing microtome (Leica SM2010R), stained with DAPI (1:1,000 dilution in PBST), and mounted on slides with ProLong Diamond Antifade Mountant (Invitrogen). For immunostaining, the fixed sections were permeabilized with 70% methanol for 15 min before blocking with 5% normal donkey serum in PBS for 1 h and incubated with primary antibodies overnight at 4 °C. Sections were washed three times in PBS and incubated with appropriate secondary antibodies overnight at 4 °C. Afterward, coverslips were mounted using ProLong Diamond Antifade mounting medium for image collection. Primary and secondary antibodies include rabbit polyclonal anti-NeuN (Millipore ABN78), rabbit polyclonal anti-Iba1 (Wako, 019-19741), rabbit polyclonal anti-Olig2 (Millipore, AB9610) and mouse monoclonal anti-GFAP (Millipore MAB360), Alexa Fluor 647 donkey anti-rabbit IgG (Jackson ImmunoResearch, cat. no. 711-606-152), Alexa Fluor 647 donkey anti-mouse IgG (Jackson ImmunoResearch, cat. no. 715-606-151), and DAPI (Cayman Chemical, cat. no. 28718-90-3). For immunohistochemistry staining, epifluorescent images were obtained at room temperature on a Nikon Eclipse T*i* microscope using a Nikon ×4 (NA 0.13, dry), ×10 (NA 0.30, dry) or ×20 (NA 0.45, dry) objectives with the same settings and configurations for each objective across all samples within each experiment.

Western blot. Protein lysates were prepared from 15–30 mg of micro-dissected brain tissue. Tissue samples were homogenized using a 27G syringe in 500 µl ml^{-1} ice-cold Pierce RIPA buffer (Thermo Fisher, cat. no. 89900) with one tablet of Roche cOmplete EDTA-free protease inhibitor (Millipore Sigma, cat. no. 11873580001). and rotated end-over-end at 4 °C for 1 h before centrifuging at 20,000*g* for 15 min at 4 °C. The supernatant was removed and quantified using Pierce BCA assay kit (Thermo Fisher, cat. no. A55864) following the manufacturer's instructions. Then, 20 µg of protein was loaded into a 4–20% SDS–PAGE gel (Bio-Rad, cat. no. 4561094), and samples were separated via electrophoresis in 1× Tris/Tricine/SDS running buffer (Bio-Rad, cat. no. 1610744) and transferred onto a PVDF membrane (Millipore, cat. no. IPVH00010) with Towbin buffer consisting of 1× Tris/glycine buffer (Bio-Rad, cat. no. 1610734) and 20% methanol using a wet transfer system (Bio-Rad, cat. no. 1703930) at 4 °C for 1 h at 100 V. Following transfer, the membrane was washed in 100% methanol for 1 min, rinsed with milliQ H_2O, wet with 1× PBS for 2 min, and then incubated shaking in LI-COR PBST blocking solution (cat. no. 927-70001) for 1 h at room temperature. Incubation with primary antibodies was performed overnight on a shaker (60 rpm) at 4 °C in LI-COR TBS-T Block (cat. no. 927-60001) with 0.2% Tween-20 using the following primary antibodies: rabbit anti-Homer1b/c (Synaptic Systems, cat. no. 160018, 1:2,000 dilution) and biotinylated mouse anti-NeuN (Millipore Sigma, cat. no. MAB377B, 1:2,000 dilution). The membrane was washed with 0.2% PBST 3× for 5 min at room temperature while shaking (60 rpm), then incubated for 1 h shaking at room temperature in LI-COR TBS-T Block with 0.2% Tween-20 and 0.1% SDS containing the following secondary antibodies: donkey anti-rabbit 800CW (LI-COR, cat. no. 926-32213, 1:1,500 dilution) and streptavidin-680RD (LI-COR, cat. no. 926-68079, 1:15,000 dilution) in the dark. The membrane was washed 4× for 5 min in 1% PBST, then 1× for 5 min in PBS, allowed to dry and then imaged on a LI-COR Odyssey.

Single-cell sequencing. *Single-cell dissociation and single-cell RNA sequencing*. Single-cell suspensions of PFC were prepared as described previously[40]. In brief, mice were killed with an overdose of isoflurane, followed by transcardial perfusion with carbogenated (95% O_2 and 5% CO_2) Hanks' balanced salt solution. Brains were removed, 500-µm sections were collected and the PFC region was isolated. The tissue was dissociated using papain (LS003124, Worthington) dissolved in Hibernate A buffer (NC1787837, Fisher Scientific) and incubated for 25–30 min at 37 °C, followed by manual trituration using fire polished Pasteur pipettes and filtering through a 40-µm cell strainer (BAH136800040, Millipore Sigma). Cells were washed with wash buffer (PBS + 1% BSA) and centrifuged at 200*g* for 5 min, the supernatant was carefully removed, and cells were resuspended in ~500 µl wash buffer and 10% DAPI. Flow cytometry was conducted using a BD FACS Aria III Cell Sorter (BD FACSDiva software, v.8.0.1) with a 100-µm nozzle. The cell suspensions were first gated on forward scatter, then within this population, based on lack of DAPI staining (Supplementary Fig. 2a,b). Cells were collected in wash buffer, manually counted using a Burker chamber, and suspension volumes were adjusted to a target concentration of 700–1,000 cells per µl. The scRNA-seq was carried out with the Chromium Next GEM Single Cell 3′ kit v.3.1 (10x Genomics, 1000268). Manufacturer's instructions were followed for downstream cDNA synthesis (12–14 PCR cycles) and library preparation. Final libraries were sequenced on the Illumina NovaSeq S4 platform (R1, 28 cycles, i7, 8 cycles and R2, 90 cycles).

Single-cell RNA sequencing data analysis. RAW sequencing reads were aligned to the GRCm38/mm10 mouse reference genome and processed with default parameters for the 10x single-cell 3′ library using a custom Sequence Quality Control (SEQC)[87] pipeline, which performs multimapped read resolution and unique molecular identifier (UMI) correction to output a cell-by-gene count matrix for each sample. The custom pipeline also distinguishes cells from empty droplets, removes cells with high mitochondrial content (>20%) and removes cells expressing few unique genes. Viable cells were identified based on library size and complexity, whereas cells with >20% of transcripts derived from mitochondria were excluded from further analysis. The Python Scanpy package[88] (v.1.9.3) was used to analyze the data further. Replicates were merged and doublets were removed using Scrublet[89]. Cells with <2,500 UMIs per cell, cells with <1,000 genes and genes detected in <3 cells were removed. Per-cell counts were normalized to equal the median of total counts per cell and $\log_2$-transformed. Principal-component analysis was used to reduce the dimensionality to 50 principal components. A nearest-neighbor graph was computed between cells using these principal components, and Leiden clustering was applied to separate the cells into distinct clusters of major cell types. Known gene markers were used[40] to assign cell types. Once the neuronal cluster was identified, it was subsetted and re-clustered using the first 50 principal components to identify inhibitory and excitatory neurons. Clusters containing fewer than ten cells from any line or condition were excluded. Clusters with differential *Homer1* expression between cc083 and cc025 strains were identified using *t*-tests. Clusters with significantly different *Homer1* expression between strains were merged, and the 'MAST' R package[44] was used to identify DE genes between strains for the merged cluster as well as all individual clusters. Cells were grouped by expression profiles performed on the same expression matrix subsequently used for testing. Consequently, cluster-wise comparisons are post-selection: the cluster definitions and tested contrasts are not independent of the data, and across-cluster multiple-comparison procedures do not strictly control error in this setting and can be overly conservative. We therefore treat these analyses as cluster-conditional, emphasizing effect sizes and 95% confidence intervals rather than across-cluster adjusted *P* values. Gene set enrichment analysis (GSEA) was performed using the fast GSEA package (fgsea v.1.18.0), the GO_Molecular_Function_2021 gene set and the Elsevier_Pathway_Collection gene set libraries using Enrichr[46,90,91]. Normalized fold change values were shuffled 10,000× before gene set correlation analysis. Cortical layers were determined using the following marker genes: layer 2/3: *HTR7*, *S1PR3*, *GRM2*, *ADRA1D*, *RASGRF2*, *CALB1*; layer 4: *HTR7*, *S1PR3*, *GRM2*, *ADRA1D*, *NECAB1* and *RORB*; layer 5: *ADRA1B*, *PTGER4*, *HRH3*, *GABRG1*, *GRIK2*, *PCP4*, *CNTN6*. *MAP1B*, *CTIP2* and *ER81*; and layer 6/6b: *HTR1F*, *CHRA4*, *GLRA2*, *GRIK3*, *NTSR1*, *RXFP1*, *FOXP2*, *TLE4*, *CTGF* and *TRB1* (ref. 40).

In vivo multisite photometry recordings. *Photometry setup*. A custom dual-color, multifiber photometry setup was built. For GCaMP6f imaging, excitation of the 470 nm (imaging) and 405 nm (isosbestic control) wavelengths were provided by LEDs (Thorlabs M470F3, M405FP1), which were collimated into a dichroic mirror holder with a 425 nm long pass filter (Thorlabs DMLP425R). This was coupled to another dichroic mirror holder with a 495 nm long pass dichroic (Semrock FF495-Di02-25 × 36), which redirected the excitation light on to a custom branching low-autofluorescence fiberoptic patchcord of three bundled 400 mm diameter 0.57 NA fibers (BFP(3)_400/440/PKMJ-0.57_1m_SMA-3xFC_LAF, Doric Lenses) using a ×20/0.5 NA objective lens (Nikon CFI SFluor ×20, product no. MRF00100). GCaMP6f fluorescence from neurons below the fiber tip in the brain was transmitted via this same cable back to the mini-cube, where it was passed through a GFP emission filter (Semrock FF01-520/35-25), amplified and focused onto a high-sensitivity sCMOS camera (Prime 95b, Photometrics). For jRGECO1a imaging, a second light path was built so that excitation of the 565 nm (imaging) and 470 nm (isosbestic control) wavelengths were provided by LEDs (Thorlabs M565F3[h], M470F3), which were collimated into a dichroic mirror holder with a 505 nm long pass dichroic (Thorlabs DMLP505R). This was coupled to another dichroic mirror holder with a 573 nm long pass dichroic (Semrock Di02-R561-25 × 36), which redirected the excitation light on to a low-autofluorescence monofiberoptic patchcord with a 400-mm diameter 0.57 NA fiber (MFP_400/440/PKMJ-0.57_1m_SMA-FC_LAF, Doric Lenses) using a ×20/0.5 NA objective lens (Nikon CFI SFluor ×20, product no. MRF00100). jRGECO1a fluorescence from neurons below the fiber tip in the brain was transmitted via this same cable back to the mini-cube, where it was passed through a RFP emission filter (Semrock FF01-607/36-25), amplified and focused onto a high-sensitivity CMOS camera (BFS-PGE-50S5M-C, Teledyne FLIR).

Each of the multiple branch ends of the branching fiberoptic patchcord as well as the monofiberoptic patchchord were coupled to four 2-m low-autofluorescence patchcords (MFP_400/430/1100-0.57_2m_FCZF1.25_LAF, Doric Lenses), which were used to collect emission fluorescence from 1.25-mm diameter lightweight ferrules (MFC_400/430-0.48_ZF1.25, Doric Lenses) using a mating sleeve (SLEEVE_BR_1.25, Doric Lenses). A microcontroller (Arduino Uno) was programmed to take trigger inputs from the Operant Behavior Setup or MATLAB and synchronize the camera shutters and alternate triggering of the 405 nm and 565 nm LEDs together and both 470 nm LEDs together. Custom TTL converters were used to read in-frame acquisition times to the Habitest Modular system (described above), which were integrated with events from the behavior in Graphic State 4. Bulk activity signals were collected using the PVCAM (GCaMP) and Spinnaker (jRGECO) software and data were further post-processed and analyzed using custom MATLAB scripts.

Quantification and statistical analysis. Data distributions were assumed to be normal, but this was not formally tested.

Behavior statistical reporting. Sample sizes were selected based on expected variance and effect sizes from the existing literature, and no statistical methods were used to determine sample size a priori. Before experiments being performed, mice were randomly assigned to experimental or control groups. The investigator was blinded to all behavioral studies (except for CC083 versus CC025 cohorts, where coat color differences prevent blinding during experimentation). *Homer1a*/*Ania3* shRNA mice were removed from the developmental knockdown experiments if they did not have sufficiently reduced expression relative to the Scramble groups or were extreme outliers from the remainder of the knockdown mice. Data analyses for calcium imaging were automated using MATLAB scripts. Statistical tests were performed in MATLAB 2022b or GraphPad Prism v.9.

Gene expression statistics. Differential gene expression between high- and low-performing DO mice as well as between CC025 and CC083 mice from bulk RNA-seq data was determined in R (v.3.5.0) using the DESeq2. *P* values were determined using a Wald test and *P* values were corrected using the Benjamini–Hochberg method.

Multifiber photometry data processing. For analysis, the images captured by the sCMOS camera were post-processed using custom MATLAB scripts. Regions of interest were manually drawn for each fiber to extract fluorescence values throughout the experiment. The 405 nm (GCaMP) or 470 nm (jRGECO) reference traces were scaled to best fit the 470 nm (GCaMP) or 565 nm (jRGECO) signal using least-squares regression. The normalized change in fluorescence (dF/F) was calculated by subtracting the scaled 405 nm or 470 nm reference traces from the 470 nm or 565 nm signals, respectively, and dividing those values by the scaled reference traces. This normalization to the isosbestic signal is carried out to adjust for bleaching and motion artifacts. Then, the true baseline of each dF/F trace was determined and corrected by using the MATLAB function 'msbackadj' estimating the baseline over a 200-frame sliding window, regressing varying baseline values to the window's data points using a spline approximation, and adjusting the baseline in the peak range of the dF/F signal. Task events (for example, cue on/offsets and nosepokes), were time stamped via Graphic State 4 software.

Multifiber photometry data analysis. Total mean activity for different task phases and different strains was quantified as an area under the curve (AUC) of dF/F responses shifted above 0. The AUC was calculated using MATLAB's 'trapz' function and normalized with the recorded time. A Pearson correlation of the dF/F responses was performed between different regions using the 'corr' (MATLAB) function. To ensure that correlation values were significantly more than chance, each timeseries was scrambled 10,000 times randomly, for each session across all mice. All such chance correlation coefficients were pooled to calculate mean (all of which were at or near zero) and standard deviation of chance correlations. To quantify the SNR, we calculated the mean and standard deviation of each region's neural activity (dF/F) during baseline periods of the task (all omission trials, from cue onset to the onset of the pre-trial delay phase, calculated values referred to as baseline mean and baseline s.d.) for each mouse for a given day. Trial SNR was calculated as the difference between the maximum pre-cue activity (dF/F for the 5 s immediately before cue onset) and the mean-baseline value for that mouse, divided by the baseline s.d. value ((trial pre-cue maximum − baseline mean)/baseline s.d.). For cohorts that progressed to the 1-s cue training phase, only mice remaining above 70% performance accuracy were included in the analyses. Additionally, the first training session and any training sessions under 15-min long were not included in the analyses. For cohorts that did not progress to the 1-s cue training phase, outliers were removed using the ROUT method with $Q = 1\%$ to account for large variations in behavioral performance.

Reporting summary

Further information on research design is available in the Nature Portfolio Reporting Summary linked to this article.

References

75. Kang, H. M. et al. Variance component model to account for sample structure in genome-wide association studies. *Nat. Genet.* **42**, 348–354 (2010).
76. Keele, G. R. et al. Integrative QTL analysis of gene expression and chromatin accessibility identifies multi-tissue patterns of genetic regulation. *PLoS Genet.* **16**, e1008537 (2020).
77. Zhang, Z., Wang, W. & Valdar, W. Bayesian modeling of haplotype effects in multiparent populations. *Genetics* **198**, 139–156 (2014).
78. Jin, J. et al. Cholinergic neurons of the medial septum are crucial for sensorimotor gating. *J. Neurosci.* **39**, 5234–5242 (2019).
79. Lister, R. G. The use of a plus-maze to measure anxiety in the mouse. *Psychopharmacology* **92**, 180–185 (1987).
80. Dobin, A. et al. STAR: ultrafast universal RNA-seq aligner. *Bioinformatics* **29**, 15–21 (2013).
81. Patro, R., Duggal, G., Love, M. I., Irizarry, R. A. & Kingsford, C. Salmon provides fast and bias-aware quantification of transcript expression. *Nat. Methods* **14**, 417–419 (2017).
82. Love, M. I., Huber, W. & Anders, S. Moderated estimation of fold change and dispersion for RNA-seq data with DESeq2. *Genome Biol.* **15**, 550 (2014).
83. Che, A. et al. Layer I interneurons sharpen sensory maps during neonatal development. *Neuron* **99**, 98–116.e7 (2018).
84. Dana, H. et al. Sensitive red protein calcium indicators for imaging neural activity. *eLife* **5**, e12727 (2016).
85. Chen, T.-W. et al. Ultrasensitive fluorescent proteins for imaging neuronal activity. *Nature* **499**, 295–300 (2013).
86. Powell, S. K. et al. Characterization of a novel adeno-associated viral vector with preferential oligodendrocyte tropism. *Gene Ther.* **23**, 807–814 (2016).
87. Azizi, E. et al. Single-cell map of diverse immune phenotypes in the breast tumor microenvironment. *Cell* **174**, 1293–1308 e36 (2018).
88. Wolf, F. A., Angerer, P. & Theis, F. J. SCANPY: large-scale single-cell gene expression data analysis. *Genome Biol.* **19**, 15 (2018).
89. Wolock, S. L., Lopez, R. & Klein, A. M. Scrublet: computational identification of cell doublets in single-cell transcriptomic data. *Cell Syst.* **8**, 281–291 e9 (2019).
90. Chen, E. Y. et al. Enrichr: interactive and collaborative HTML5 gene list enrichment analysis tool. *BMC Bioinform.* **14**, 128 (2013).
91. Kuleshov, M. V. et al. Enrichr: a comprehensive gene set enrichment analysis web server 2016 update. *Nucleic Acids Res.* **44**, W90–W97 (2016).

Acknowledgements

We thank the Rajasethupathy laboratory members for helpful discussions throughout. We thank J. Hudspeth for advice on testing auditory brainstem responses. We thank C. Bargmann, J. Friedman and R. Lifton for helpful discussions related to genetics and genetic mapping. We thank M. B. Hatten and B. Darnell for discussions related to developmental biology and *Homer1* functions. We thank P. Greengard's laboratory for sharing behavioral instrumentations and R. Sharma for suggestions on the scRNA-seq analysis. We thank J. Regalado for help with photometry experiments and analysis, J. Weisman for contributions to the dual-color photometry system, V. Li for stereotactic surgeries and J. Brandt and M. Kirylo for help with biochemistry experiments. We thank the core facilities at Rockefeller (Precision Instrumentation, Genomics, and FACS), the Memorial Sloan Kettering Cancer Center (Single Cell Analytics Innovation Laboratory) and the University of Arizona (Viral Production Core). Cartoons in some figures (Figs. 3, 4 and 6) were created with BioRender.com. This work was supported by a Kavli Institute pilot grant from The Rockefeller University (A.T.), a Medical Scientist Training Program grant from NIGMS (T32GM007739) to the Tri-Institutional MD-PhD Program (A.F.I.), and grants from the National Institutes of Health under award numbers F30HD100089 (A.F.I.), 2R01MH110553 (N.V.D.M.G.), DP2AG058487 (P.R.), as well as grants from the Pershing Foundation, Vallee Foundation and the Harold and Leila Mathers Foundation (P.R.).

Author contributions

Z.G., P.R. and P.S. conceived the study. Z.G., A.B.-O. and P.R. designed the experiments. Z.G. selected and optimized the behaviors, performed mouse behaviors (together with A.B.-O.), molecular studies including RNA preparation and single cell dissociation (together with A.T.), cloning and cell-based assays and in vivo neural activity recordings and analysis, supervised by P.R. M.K. performed QTL as well as RNA-seq analysis, supervised by P.S. A.T. assisted with designing and performing the scRNA-seq experiments and analysis. Z.G. and G.R. designed the head-fixed behaviors and G.R. performed these experiments. J.F., Y.H. and M.G. assisted with surgeries and histology. A.F.I. performed surgeries for the developmental study, supervised by N.V.D.M.G. B.F. performed auditory brainstem recordings. Z.G. and P.R. wrote the paper with input from all authors.

Competing interests

The authors declare no competing interests.

Additional information

Extended data is available for this paper at https://doi.org/10.1038/s41593-025-02155-2.

Supplementary information The online version contains supplementary material available at https://doi.org/10.1038/s41593-025-02155-2.

Correspondence and requests for materials should be addressed to Priya Rajasethupathy.

Peer review information *Nature Neuroscience* thanks Abraham Palmer, Vikaas Sohal, Paul Worley and the other, anonymous, reviewer(s) for their contribution to the peer review of this work.

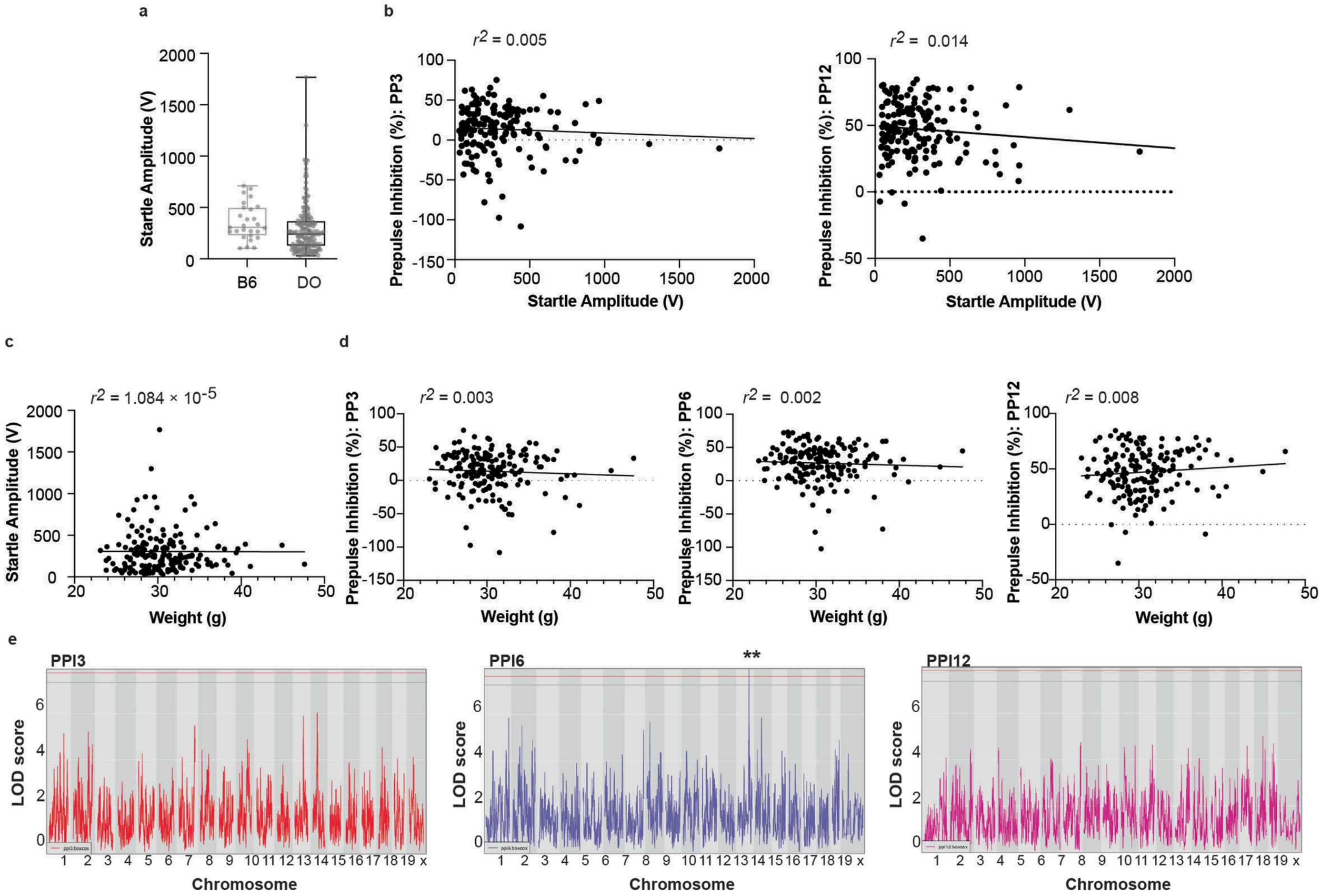

Extended Data Fig. 1 | Additional genetic and behavioral characterization of DO mice. Related to Fig. 1. **a**, Startle response assessed during PPI experiments in B6 (gray, *n* = 27) and DO (black, *n* = 176) mice measured as startle amplitude (V). Upper and lower box limits indicate 75th and 25th percentiles, centerline indicates the median, upper and lower whiskers are the maximum and minimum data points. **b**-**d**, Correlations in DO mice (*n* = 176) between (**b**) startle response, measured as the magnitude of startle amplitude (V), and PPI, measured as percent inhibition, at 3 (PP3, $r^2 = 0.005$) and 12 (PP12, $r^2 = 0.014$) dB above background, (**c**) weight and startle response ($r^2 = 1.084 \times 10^{-5}$), and (**d**) weight and PPI (PP3, $r^2 = 0.003$; PP6, $r^2 = 0.002$; PP12, $r^2 = 0.008$) dB above background. **e**, QTL mapping analysis (by R/qtl2), shown as Manhattan plots, of PPI at 3 (PPI3, red), 6 (PPI6, purple, genome-wide $p < 0.01$), and 12 dB (PPI12, magenta) above background (*n* = 176; blue lines indicate 90% confidence threshold and red lines indicate 95% confidence threshold).

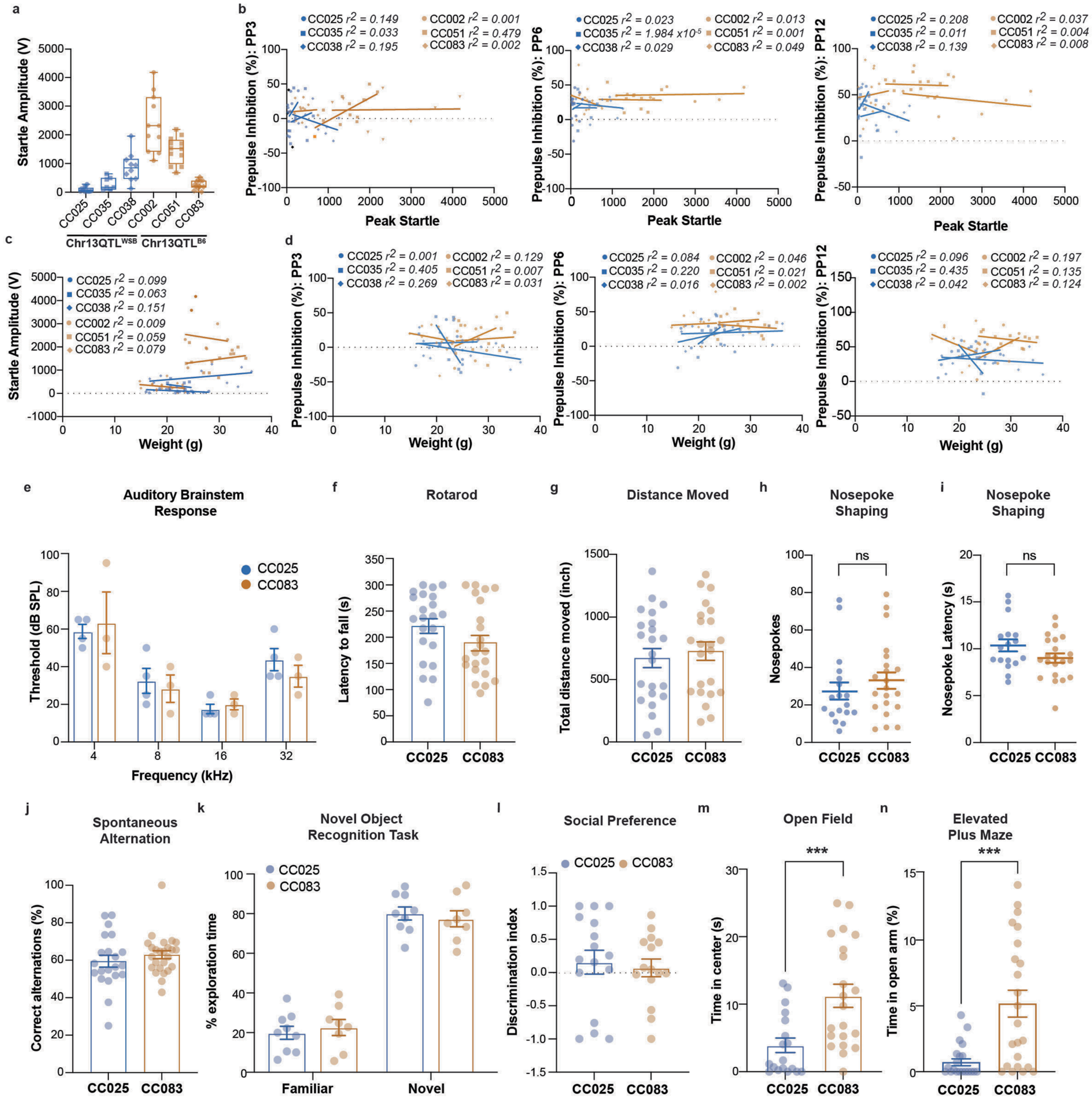

Extended Data Fig. 2 | See next page for caption.

Extended Data Fig. 2 | Behavioral phenotype and covariate characterization of CC083 and CC025 mice. Related to Fig. 2. **a**, Startle response, measured as the magnitude of the startle amplitude (V) in three CC lines with the Chr13 QTL^{WSB} (low-performing) diplotype, CC025 (*n* = 7 M + 7 F), CC035 (*n* = 6 M + 3 F), and CC038 (*n* = 6 M + 6 F), and three CC lines with the Chr13 QTL^{B6} (high-performing) diplotype, CC002 (*n* = 6 M + 6 F), CC051 (*n* = 6 M + 6 F), and CC083 (*n* = 7 M + 7 F), two-sided Welch-corrected t-test between haplotypes $p < 0.001$. Upper and lower box limits indicate 75th and 25th percentiles, centerline indicates the median, upper and lower whiskers are the maximum and minimum data points. No significant interaction between sex and CC line by two-way ANOVA. **b**-**d**, Correlations in three CC lines with the Chr13 QTL^{WSB} (low-performing) diplotype, CC025 (*n* = 7 M + 7 F), CC035 (*n* = 6 M + 3 F), and CC038 (*n* = 6 M + 6 F), and three CC lines with the Chr13 QTL^{B6} (high-performing) diplotype, CC002 (*n* = 6 M + 6 F), CC051 (*n* = 6 M + 6 F), and CC083 (*n* = 7 M + 7 F) between (**b**) startle response and PPI, measured as percent inhibition, at 3 dB (PP3), 6 dB (PP6), and 12 dB (PP12) above background, (**c**) weight and startle response, and (**d**) weight and PPI. **e**, Auditory brainstem response measured as minimum thresholds in CC025 (*n* = 3 M + 1 F) and CC083 (*n* = 2 M + 1 F) as sound pressure level (dB) in response to increasing frequencies (4, 8, 16, 32 kHz). **f**, Motor coordination measured in CC025 (*n* = 10 M + 12 F) and CC083 (*n* = 10 M + 12 F) as latency (s) to fall from the rod in the Rotarod test averaged across 4 consecutive trials. Significant difference between sexes but no significant interaction between sex and CC line by two-way ANOVA. **g**, Gross motor activity measured in CC025 (*n* = 11 M + 12 F) and CC083 (*n* = 11 M + 12 F) mice as total distance moved (inch) in a square open field arena during a 5-min test. Significant difference between sexes but no significant interaction between sex and CC line by two-way ANOVA. **h**-**i**, Performance of CC025 (*n* = 8 M + 10 F) and CC083 (*n* = 9 M + 12 F) mice during nosepoke shaping, where the motor activities required are the same as the SDT training but with no attentional component (that is cue), showing (**h**) the number of nosepokes per mouse on the day of nosepoke shaping when the mice met criteria to proceed to SDT training and (**i**) the average latency to nosepoke after retrieving a reward for each mouse that retrieved rewards on the first nosepoke shaping day. No significant interaction was found between sex and CC line by two-way ANOVA. **j**, Working memory performance assessed during a spontaneous alternation task in a Y-maze apparatus for CC025 (*n* = 9 M + 12 F) and CC083 (*n* = 13 M + 12 F) mice, measured as the percent of correct alternations (Methods). No significant interaction between sex and CC line by two-way ANOVA. **k**, Short-term memory tested by a novel object recognition test in CC025 (*n* = 9 M) and CC083 (*n* = 10 M) mice, measured as time spent exploring the novel object *vs* the familiar one and expressed as the percentage of total exploration time during a 5 min test. Two-way ANOVA showed a significant main effect for novelty ($p < 0.0001$), but not for CC line. **l**, Social behavior for CC025 (*n* = 9 M + 7 F) and CC083 (*n* = 8 M + 7 F) mice, expressed as discrimination index determined by exploration time in a 3-chamber social interaction test. Significant difference between sexes but no significant interaction between sex and CC line by two-way ANOVA. **m**, Anxiety-like behavior measured as time, in seconds, spent in the center of an open field arena during a 5 min test in CC025 (*n* = 8 M + 10 F) and CC083 (*n* = 11 M + 10 F). Significant main effects for CC line ($p = 0.0007$) and sexes ($p = 0.0005$) but no significant interaction between sex and CC line by two-way ANOVA. **n**, Anxiety-like behavior measured as the percentage of time spent in the open arm of an elevated plus maze during a 5-min test in CC025 (*n* = 9 M + 10 F) and CC083 (*n* = 11 M + 12 F) mice. Significant main effect for CC line ($p = 0.0006$) but no significant sex effect or interaction between sex and CC line by two-way ANOVA. Data in **e**-**n** are shown as mean ± SEM.

https://doi.org/10.1038/s41593-025-02155-2

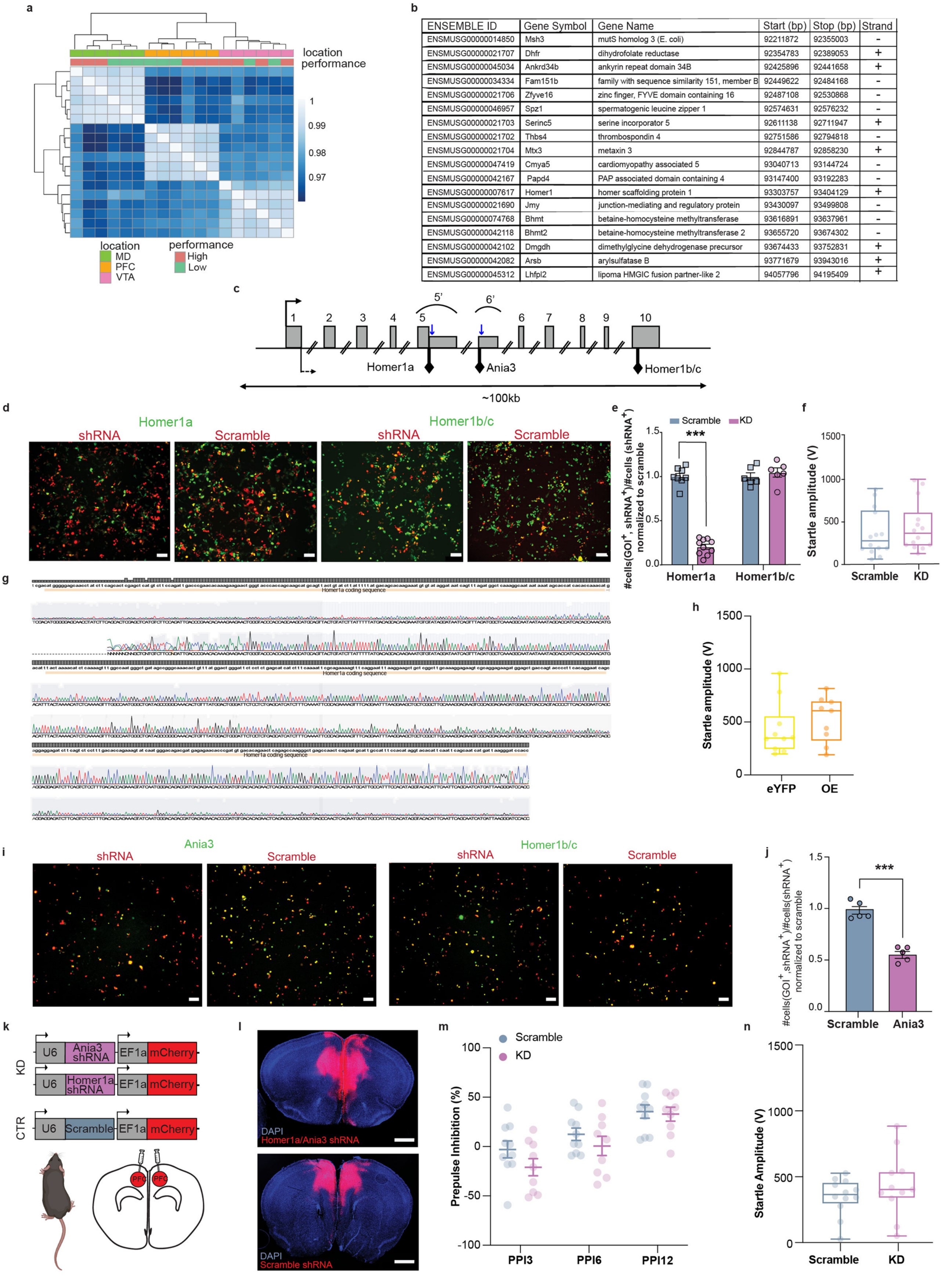

ENSEMBLE ID	Gene Symbol	Gene Name	Start (bp)	Stop (bp)	Strand
ENSMUSG00000014850	Msh3	mutS homolog 3 (E. coli)	92211872	92355003	-
ENSMUSG00000021707	Dhfr	dihydrofolate reductase	92354783	92389053	+
ENSMUSG00000045034	Ankrd34b	ankyrin repeat domain 34B	92425896	92441658	+
ENSMUSG00000034334	Fam151b	family with sequence similarity 151, member B	92449622	92484168	-
ENSMUSG00000021706	Zfyve16	zinc finger, FYVE domain containing 16	92487108	92530868	-
ENSMUSG00000046957	Spz1	spermatogenic leucine zipper 1	92574631	92576232	-
ENSMUSG00000021703	Serinc5	serine incorporator 5	92611138	92711947	+
ENSMUSG00000021702	Thbs4	thrombospondin 4	92751586	92794818	-
ENSMUSG00000021704	Mtx3	metaxin 3	92844787	92858230	+
ENSMUSG00000047419	Cmya5	cardiomyopathy associated 5	93040713	93144724	-
ENSMUSG00000042167	Papd4	PAP associated domain containing 4	93147400	93192283	-
ENSMUSG00000007617	Homer1	homer scaffolding protein 1	93303757	93404129	+
ENSMUSG00000021690	Jmy	junction-mediating and regulatory protein	93430097	93499808	-
ENSMUSG00000074768	Bhmt	betaine-homocysteine methyltransferase	93616891	93637961	-
ENSMUSG00000042118	Bhmt2	betaine-homocysteine methyltransferase 2	93655720	93674302	-
ENSMUSG00000042102	Dmgdh	dimethylglycine dehydrogenase precursor	93674433	93752831	+
ENSMUSG00000042082	Arsb	arylsulfatase B	93771679	93943016	+
ENSMUSG00000045312	Lhfpl2	lipoma HMGIC fusion partner-like 2	94057796	94195409	+

Extended Data Fig. 3 | See next page for caption.

Extended Data Fig. 3 | Further DO RNA-seq information, *Homer1* exons, *in vitro* validation & additional behavioral characterization of *Homer1* manipulations. Related to Fig. 3. **a**, Heatmap of hierarchical clustering by Euclidean distance among gene expression profiles in DO high- (pink, *n* = 3) and low- performers (green, *n* = 3) as highlighted in Fig. 3a-b and from three brain regions per mouse: mediodorsal thalamus (MD, green), prefrontal cortex (PFC, orange) and ventral tegmental area (VTA, pink). Clustering is visible by brain region and performance in MD and PFC. **b**, Table showing protein-coding genes within the 95% CI surrounding the Chr13 QTL identified by rQTL2. **c**, Schematic representation of the *Homer1* genomic exon structure. The bent arrow at the 5' end of exon 1 (solid line, above) indicates the putative transcription start site, while the bent arrow at the 3' end of exon 1 (dashed line, below) represents the translation start site. Black diamonds (below) indicate the translation stop sites of *Homer1a*, *Ania3*, and *Homer1b/c*, respectively. To create *Homer1a*, exon 5 extends into intron 5 to create the *Homer1a*-specific exon (5') through alternative splicing. *Ania3* is generated by alternative splice usage of intron 5 sequence downstream of exon 5' as the *Ania3*-specific exon 6'. (Adapted from Bottai et al. 2002). Blue arrows indicate shRNA binding locations. **d**-**e**, *in vitro* validation of *Homer1a* gene knockdown construct. **d**, Representative images of HEK cells co-transfected with *Homer1a* (first and third images from the left) or Scramble (second and fourth images from the left) shRNA (red) and *Homer1a* (first and second images from the left) or *Homer1b/c* (third and fourth images from the left) expression constructs (green). Scale bar: 100 µm. **e**, Quantification of shRNA-mediated gene knockdown, expressed as the fraction of cells co-expressing a *Homer1* isoform construct and shRNA construct relative to the total number cells expressing the shRNA construct, normalized to the respective scramble control experiments (two-way ANOVA showed significant main effects for *Homer1* isoform expression, $p < 0.0001$, and shRNA construct, $p < 0.0001$, as well as a significant interaction between those variables, $p < 0.0001$; two-sided Holm–Sidak's test for multiple comparisons showed a significant difference in *Homer1a* expression between the shRNA (purple, *n* = 10 fields of view across 2 independent experiments) and Scramble (blue, *n* = 8 fields of view across 2 independent experiments) constructs, $p < 0.0001$). **f**, Startle response in *Homer1a* KD (*n* = 14) and Scramble (*n* = 14) mice. **g**, Electropherogram of AAV-CaMKII(1.3)-Homer1a-eYFP overexpression construct aligned to the *Homer1a* coding sequence (tan bar near the top of each line). The height of gray boxes at the top of each line is proportional to the number of sequencing runs aligned to the reference sequence (maximum # of sequencing runs in image = 2). **h**, Startle response in *Homer1a* OE (*n* = 9) and control eYFP (*n* = 10) mice. **i**, Representative images of HEK cells co-transfected with *Ania3* (first and third images from the left) or Scramble (second and fourth images from the left) shRNA (red) and *Ania3* (first and second images from the left) or *Homer1b/c* (third and fourth images from the left) expression constructs (green), Scale bar: 100 µm. **j**, Quantification of shRNA-mediated gene knockdown, expressed as the fraction of cells co-expressing the *Ania3* expression construct and shRNA or scramble construct relative to the total number cells expressing the shRNA or scramble, normalized to the scramble control experiments. In cells transfected with the *Ania3* expression construct, there was a significant difference in *Ania3* expression between the cells co-transfected with the shRNA (*n* = 5 fields of view), and Scramble (*n* = 5 fields of view) constructs (unpaired two-sided t-test, $p < 0.0001$). **k**, Schematic of constructs and injection location (PFC) for knockdown (KD, purple) and control (Scramble, blue) in adult B6 mice. **l**, Validation histology performed 12 weeks after bilateral injection of pooled AAV-U6-Homer1a_shRNA-EF1a-mCherry and AAV-U6-Ania3_shRNA-EF1a-mCherry viruses for KD (purple, upper panel) and AAV-U6-Scramble-EF1A-mCherry control virus for Scramble (blue, lower panel) into PFC, showing viral transduction in the target area (DAPI, blue; mCherry, red). Scale bars: 1000 µm. **m**-**n**, PPI (**m**) and startle response (**n**) in Scramble (*n* = 10) and adult *Homer1a/Ania3* KD (*n* = 9) mice. Data in **e**, **j**, and **m** are expressed as mean ± SEM, and for **f**, **h**, and **n**, upper and lower box limits indicate 75th and 25th percentiles, centerline indicates the median, upper and lower whiskers are the maximum and minimum data points.

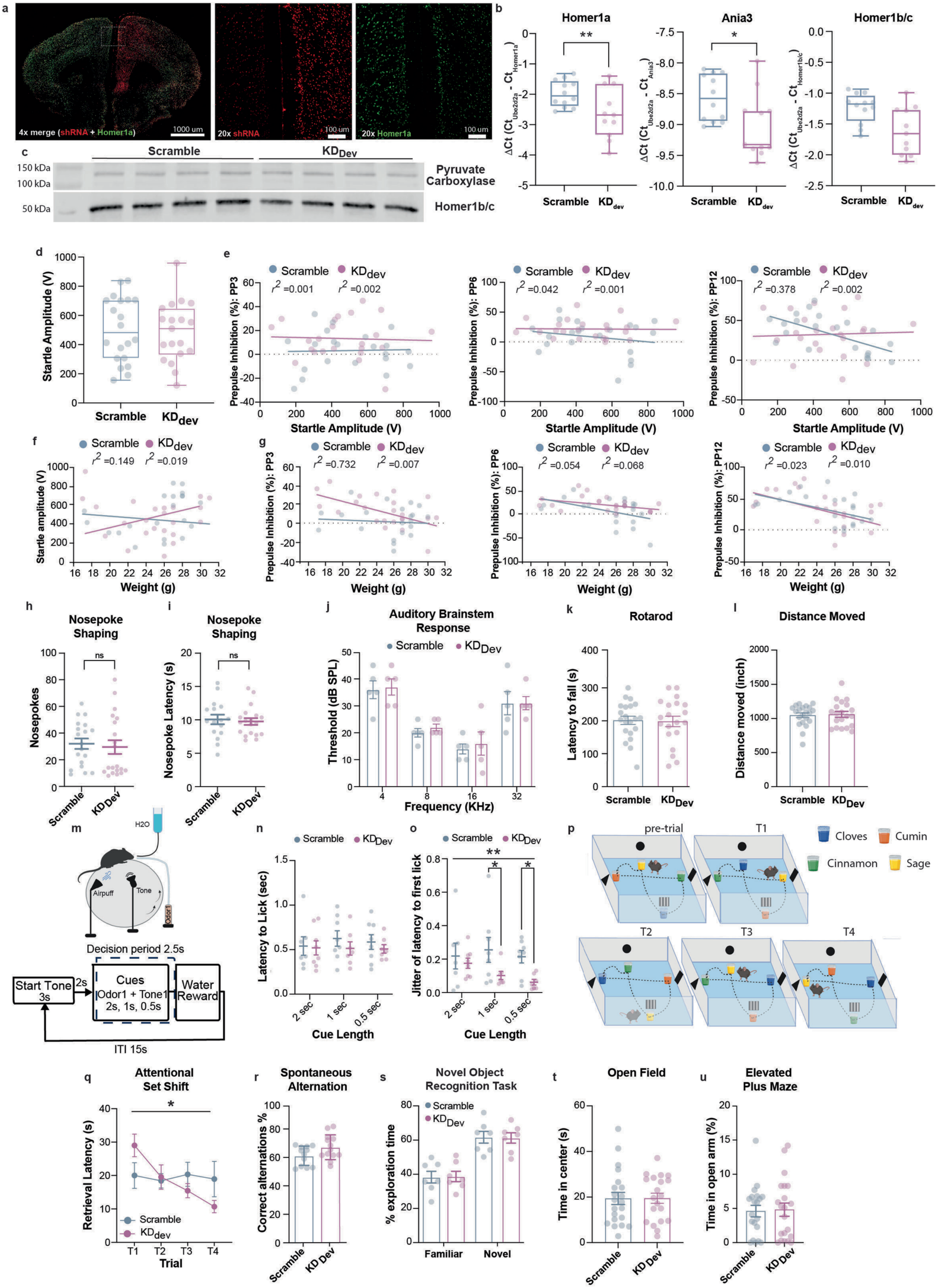

Extended Data Fig. 4 | See next page for caption.

Extended Data Fig. 4 | *In vitro* characterization of Ania3 shRNA construct and *in vivo* characterization of developmental knockdown (KD_{dev}) manipulation. Related to Fig. 4. **a**, Representative histology by *in situ* RNA hybridization of unilateral developmental knockdown injection at p15. Image is representative of 3 independent samples. Left: 4x merged image showing *Homer1a* and shRNA expression, scale bar: 1000 µm. White box indicates the region used for higher magnification images. Center: 20x image of *Homer1a* expression only (left), mCherry expression only (center), and both *Homer1a* and mCherry expression (right), scale bars: 100 µm. For all images, Homer1a is shown in green and mCherry is shown in red. **b**, *ex vivo* validation of developmental knockdown manipulation assessed by quantification of *Homer1a* (left), *Ania3* (center) and *Homer1b/c* (right) levels measured by qPCR in PFC samples dissected from Scramble (n = 12) and KD_{dev} (n = 15), (two-way ANOVA showed significant main effects for group, p < 0.0001, and *Homer1* isoform expression, p < 0.0001; post hoc Holm−Sidak's test for multiple comparisons shows a significant difference in *Homer1a*, p = 0.0038, and *Ania3*, p = 0.0451, expression). **c**, Western blot for Homer1b/c in Scramble and KD_{dev} mice (n = 4 per group) 4 months after injection. Raw western blot images can be found in Supplementary Fig. 1. **d**, Startle response in Scramble (n = 12 M + 8 F) and KD_{dev}, (n = 10 M + 8 F). **e**-**g**, Correlations between (**e**) startle response and PPI, measured as percent inhibition, at 3 dB (PP3), 6 dB (PP6), and 12 dB (PP12) above background, (**f**) weight (g) and startle response, and (**g**) weight and PPI. **h**-**i**, Performance during nosepoke shaping, where the motor activities required are the same as the SDT training but with no attentional component (that is cue) for scramble (n = 12 M + 7 F) and KD_{dev} (n = 12 M + 8 F) mice, showing (**h**) the number of nosepokes per mouse on the day of nosepoke shaping when the mice met criteria to proceed to SDT training and (**i**) the average latency to nosepoke after retrieving a reward for each mouse that retrieved rewards on the first nosepoke shaping day. No significant interaction between sex and group by two-way ANOVA.**j**, Auditory brainstem response measured as minimum thresholds in Scramble (n = 4 M + 1 F) and KD_{dev} (n = 4 M + 1 female), as sound pressure level (dB) in response to increasing frequencies (4, 8, 16, 32 kHz). **k**, Motor coordination in the Rotarod test for Scramble (n = 13 M + 8 F) and KD_{dev} (n = 12 M + 8 F), measured as latency (s) to fall from the rod averaged across 4 consecutive trials. Significant difference between sexes but no significant interaction between sex and group by two-way ANOVA. **l**, Gross motor activity measured as distance moved (inch) by Scramble (n = 13 M + 8 F) and KD_{dev} (n = 12 M + 8 F) in a square open field arena during a 5-min test. **m**, Schematic of head-fixed SDT setup (left) and task structure (right). **n**, Quantification of the latency to first lick (sec) within the decision windows across cue lengths. Each point is the average latency to first lick for the first 3 Go trials per animal (2 s cue: Scramble n = 7 M, KD_{dev} n = 8 M; 1 s and 0.5 s cues: Scramble n = 8 M, KD_{dev} n = 7 M). **o**, Quantification of the latency to first lick jitter across cue lengths. Jitter is quantified as the standard deviation of first lick latencies across the first 3 Go trials (two-way ANOVA showed a significant main effect for group, p = 0.007, and post hoc Holm−Sidak's test for multiple comparisons showed significant differences between groups at 1 and 0.5 s cues, p = 0.04 for both cue lengths, 2 s cue: Scramble n = 7 M, KD_{dev} n = 8 M; 1 s and 0.5 s cues: Scramble n = 8 M, KD_{dev} n = 7 M). **p**, Schematic of the Attentional Set Shift setup and experiment protocol. **q**, Latency (s) to retrieve the chocolate pellet measured in Scramble (n = 14 M) and KD_{dev}, (n = 13 M) mice during the 4 trials of the Attentional Set Shift test. Significant interaction between trial and group, p = 0.04, by repeated-measures two-way ANOVA. **r**, Working memory performance assessed in a Y-maze apparatus for Scramble (n = 12 M + 7 F) and KD_{dev}, (n = 13 M + 8 F) mice, measured as correct alternations performed, expressed as a percentage total alternations. Significant difference between sexes but no significant interaction between sex and group by two-way ANOVA. **s**, Short-term memory tested by a novel object recognition test in Scramble (n = 7 M) and KD_{dev}, (n = 7 M) mice, measured as time spent exploring the novel object *vs* the familiar one and expressed as a percentage of total exploration time during a 5 min test. significant main effect for novelty (p < 0.001), but not for group by two-way ANOVA. **t**-**u**, Anxiety-like behavior measured as (**t**) time (in seconds) spent in the center of an open field arena during a 5 min test in Scramble (n = 13 M + 8 F) and KD_{dev}, (n = 12 M + 8 F) mice, and (**u**) percentage of time spent in the open arm of an elevated plus maze during a 5 min test in Scramble (n = 12 M + 8 F) and KD_{dev}, (n = 13 M + 8 F) mice. Significant difference between sexes but no significant interaction between sex and group by two-way ANOVA for both **t** and **u**. Data in **h**-**l**, **n**-**o**, and **q**-**u** are expressed as mean ± SEM, and for **b** and **d**, upper and lower box limits indicate 75th and 25th percentiles, centerline indicates the median, upper and lower whiskers are the maximum and minimum data points.

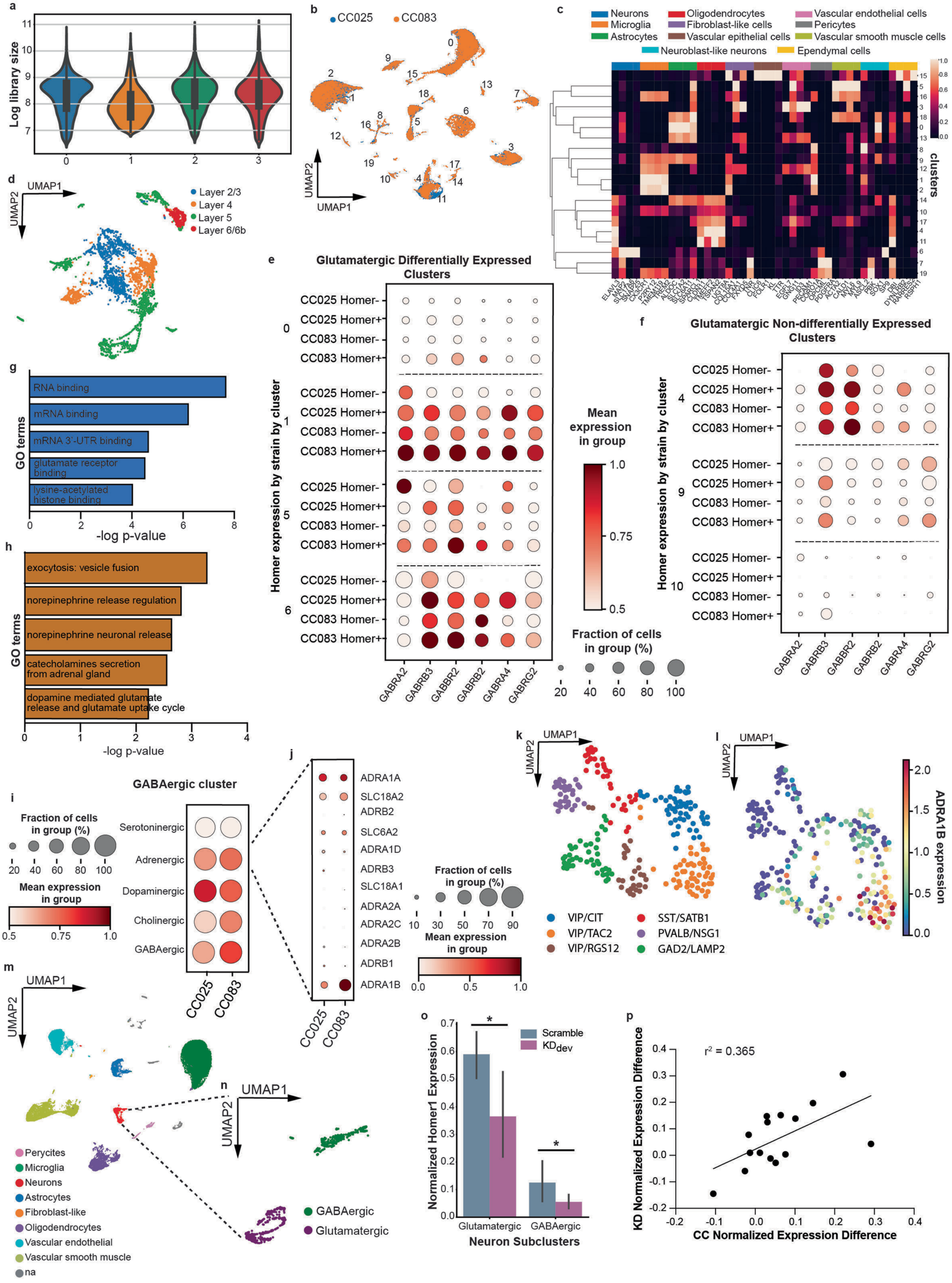

Extended Data Fig. 5 | See next page for caption.

https://doi.org/10.1038/s41593-025-02155-2

Extended Data Fig. 5 | Additional information for scRNA-seq experiments. Related to Fig. 5. **a**, Violin Plots of library size for each biological replicate (0=pooled CC025 sample 1, 1=pooled CC083 sample 1, 2=pooled CC025 sample 2, 3=pooled CC083 sample 2). Box-and-whiskers depict the median and interquartile range, lower bound = 25th percentile, center = median, upper bound = 75th percentile, lower whisker = smallest data point ≥ (Q1 - 1.5 x IQR), upper whisker = largest data point ≤ (Q3 + 1.5 x IQR). **b**, UMAP visualization of initial clusters colored by line. **c**, Heatmap of select cell type marker genes for clusters shown in **b**. **d**, Identification of the cortical layers neuron clusters likely belong to based on the expression of canonical marker genes (Methods) **e**-**f**, Dot plots showing scaled expression of select GABAergic receptors driving GO analysis of genes upregulated in the CC083 glutamatergic *Homer1* differentially expressed (DE) clusters (Fig. 5h) in both the glutamatergic (**e**) DE and (**f**) non-differentially expressed clusters stratified by cluster, line, and *Homer1* positivity. **g**, Gene ontology (GO) analysis of molecular function by Enrichr for genes upregulated in CC025 cells within the glutamatergic *Homer1* differentially expressed (DE) clusters. **h**, Functional pathway enrichment analysis for CC083 cells in the GABAergic cluster using the Elsiver_Pathway_Collection gene set library in Enrichr. **i**, Dot plot showing the expression of markers for common neuromodulatory systems in GABAergic cluster 7 by line. **j**, Dot plot of adrenergic receptors and transporters in CC025 and CC083 cells in GABAergic neurons (cluster 7, Fig. 5c). **k**, UMAP visualization sub-clustering all cells identified as GABAergic neurons (cluster 7, Fig. 5c) labeled by most strongly expressed interneuron subtype marker and most highly expressed gene. **l**, UMAP visualization of scaled *ADRA1B* expression in GABAergic neuronal clusters. **m**, UMAP visualization of all cells collected from KD_{dev} and scramble mice (n = 3 mice pooled per group) clustered based on transcriptional profile. **n**, UMAP visualization sub-clustering all cells identified as neurons, identified as excitatory (glutamatergic) and inhibitory (GABAergic) neuron clusters based on expression of canonical marker genes. **o**, Differential *Homer1* expression between Scramble and KD_{dev} neurons by cluster (two-sided unpaired t-tests, glutamatergic cluster p = 0.0243 and GABAergic cluster p = 0.0249). Data shown as mean ± SD. **p**, Correlation of the normalized expression differences of GABA receptor subunit and related adaptor gene set between the CC083/CC025 and KD_{dev}/Scramble ($r^2 = 0.3653$, p = 0.017, two-sided Pearson's correlation). Genes expressed in less fewer than 20 cells in any of the groups were excluded from the analysis. For **e**-**f** and **i**-**j**, the size of each dot corresponds to the percentage of cells from each group expressing each gene or gene set, and the color intensity indicates the relative, scaled expression of the gene/gene set. For **g**-**h** raw *P*-values determined using a one-sided Fisher's exact test.

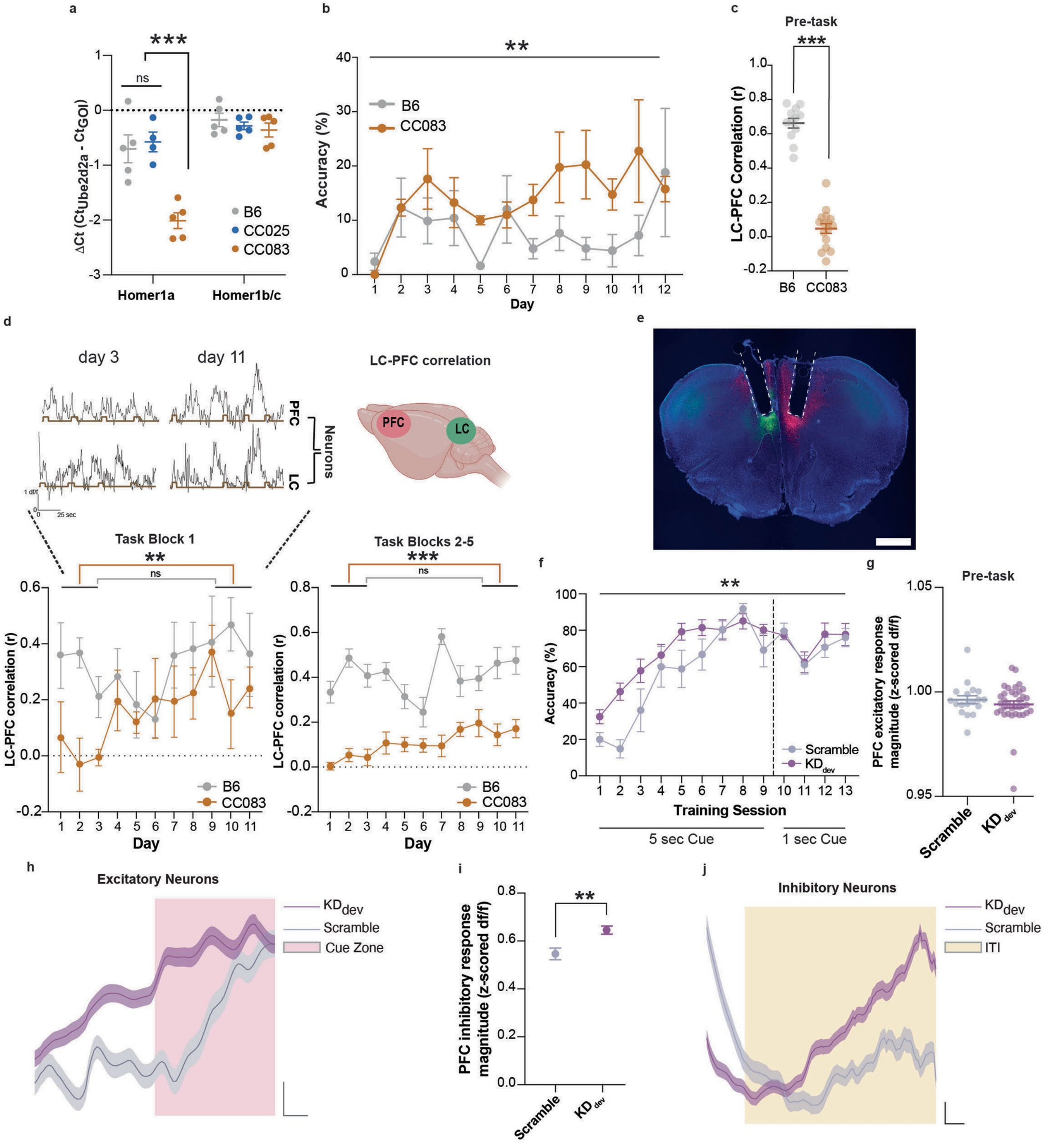

Extended Data Fig. 6 | See next page for caption.

Extended Data Fig. 6 | *Homer1* isoform expression, SDT behavioral performance, and additional photometry data. Related to Fig. 6. **a**, PFC expression of *Homer1a* and *Homer1b/c* by qPCR in B6, CC025, and CC083 adult mice (*Homer1a*: $n_{B6} = 5$, $n_{CC025} = 4$, and $n_{CC083} = 5$; *Homer1b/c:* n = 5 per line; two-way ANOVA showed significant main effects for strain, *Homer1* isoform, and a significant interaction between those variables, $p < 0.0001$ for all; post hoc Holm–Sidak's test showed significant differences for B6 *vs* CC083 and CC025 vs CC083, $p < 0.0001$ for both). **b**, Performance of B6 (n = 5) and CC083 (n = 4) mice during SDT across days showing the percentage of correct responses (two-way ANOVA, p = 0.0024). Tethering mice to fibers impacted performance for both lines equally. **c**, Pairwise Pearson's correlations between LC and PFC neuronal activity at baseline (two-sided Welch-corrected t-test for B6 *vs* CC083, n = 4 each, 5 min recordings, $p < 0.0001$). **d**, Top: representative traces from PFC (top) and LC neurons (bottom) from day 3 (left) and 11 (right), Y-axis is z-scored df/f and X-axis is time (s). Brown rectangles indicate cues. Bottom: Pairwise Pearson's correlations between LC and PFC activity during SDT sessions in B6 (n = 5) and CC083 (n = 4) mice. Each 20 min session was split into 5, 4-min blocks. Data is shown from the first 4-minute block (left) and for blocks 2–5 (right) as mean ± SEM (two-sided Welch-corrected t-tests for days 1–3 *vs* days 9-11 within strain, for CC083 p(block1)=0.003 and p(blocks 2–5) < 0.0001). **e**, Representative DAPI-stained (blue) histology image of dual-color photometry surgical preparation to simultaneously record from excitatory and inhibitory neurons in PFC by injecting AAV-mDlx-GCaMP6f (green) contralateral to AAV-CaMKII-Cre + AAV-CAG-FLEX-jRGECO1a (red) and implanting fibers above the injection site (indicated by white dashed outlines). Image is representative of 3 independent samples. Scale bar: 1000 µm. **f**, Accuracy (percentage of correct responses) for Scramble (n = 6) and KD_{dev} mice (n = 10). Two-way ANOVA showed a significant interaction between training session and group (p = 0.002). **g**, Average activity (area under responses) in home cage for Scramble (n = 6) vs KD_{dev} (n = 10) during 1 min recordings from PFC excitatory neurons. **h**, Robust trial-averaged responses from 5 seconds before to 5 seconds after cue onset for correct 5 s cue trials - 810 trials for Scramble (gray, n = 6 mice) and 1,641 trials for KD_{dev} (purple, n = 10 mice). Data are mean (dark line) and SEM (shaded area). Photometry scale: x/y: 1 s/0.1z. **i**, PFC inhibitory activity in task during the last 5 seconds of ITIs for trials on all days in Scramble (n = 6) and KD_{dev} (n = 10) mice (two-sided unpaired t-test, p = 0.001). **j**, Robust trial-averaged responses from 2 seconds before to 10 seconds after ITI onset after 5 s cue trials - 805 ITIs for Scramble (gray, n = 6 mice) and 1,634 ITIs for KD_{dev} (purple, n = 10 mice). Data are mean (dark line) and SEM (shaded area). Photometry scale: x/y: 1 s/0.05z. Data in **a**-**d**, **f**-**g**, and **i** are expressed as mean ± SEM.